Chapter I.9

Transverse nonlinear effects

Hannes Bartosik, Sofia Kostoglou
CERN, Geneva, Switzerland

This chapter provides a basic introduction to nonlinear effects in particle accelerators. It covers important concepts like resonance driving terms, resonances, tune diagram and chaotic motion, which are crucial for understanding how particle dynamics evolves in the presence of nonlinear magnetic fields. Additionally, it provides an overview of methods like resonance compensation and beam extraction. Techniques such as symplectic integration, dynamic aperture and frequency map analysis are also introduced, which are used to study and analyze these effects.

1 Introduction

This chapter provides a basic introduction to nonlinear effects in particle accelerators. It covers important concepts like resonance driving terms, resonances, tune diagram and chaotic motion, which are crucial for understanding how particle dynamics evolves in the presence of nonlinear magnetic fields. Additionally, it provides an overview of methods like resonance compensation and beam extraction. Techniques such as symplectic integration, dynamic aperture and frequency map analysis are also introduced, which are used to study and analyze these effects. More details can be found in previous works, see Refs. [1–13].

2 Example of a simple storage ring

To understand the complex beam dynamics in a particle accelerator, especially in the presence of nonlinear fields, we will start by considering a basic storage ring. We consider only the horizontal plane at this moment. This simplified lattice consists of a linear periodic transport map with $\beta_x = 1\,\mathrm{m}$ and $\alpha_x = 0$, i.e. this part of the lattice corresponds to a pure rotation in phase space

$$\begin{pmatrix} x \\ p_x \end{pmatrix} \mapsto \begin{pmatrix} \cos\mu_x & \sin\mu_x \\ -\sin\mu_x & \cos\mu_x \end{pmatrix} \begin{pmatrix} x \\ p_x \end{pmatrix}. \tag{I.9.1}$$

The lattice also includes a non-linear magnet to introduce nonlinearities in the particle trajectories. The change in the horizontal momentum of a particle moving through a sextupole is found by integrating the Lorentz force

$$\Delta p_x = -\int_0^L \frac{B_y}{B\rho}\, ds \quad \text{with} \quad \frac{B_y}{B\rho} = \frac{1}{2}k_2 x^2 \quad (\text{assuming } y = 0). \tag{I.9.2}$$

This chapter should be cited as: Transverse nonlinear effects, H. Bartosik, S. Kostoglou, DOI: 10.23730/CYRSP-2024-003.385, in: Proceedings of the Joint Universities Accelerator School (JUAS): Courses and exercises, E. Métral (ed.), CERN Yellow Reports: School Proceedings, CERN-2024-003, DOI: 10.23730/CYRSP-2024-003, p. 385.

If the sextupole is short we can neglect the small change in the coordinate x as the particle moves through the sextupole, in which case we obtain (thin lens approximation)

$$\Delta p_x = -\int_0^L \frac{1}{2} k_2 x^2 \, ds \approx -\frac{1}{2} k_2 L x^2. \tag{I.9.3}$$

The map for a particle moving through a short sextupole can be represented by a "kick" in the horizontal momentum

$$x \mapsto x,$$
$$p_x \mapsto p_x - \frac{1}{2} k_2 L x^2.$$

While this approach may appear simplistic, it allows to understand more advanced concepts, such as resonances and chaotic motion, which will be discussed in more detail in later sections.

The Python code that simulates this model is provided in Appendix A. A set of particles with increasing initial horizontal positions (vertical coordinates are set to zero for simplicity) are tracked through the lattice for several turns and their horizontal position and momentum is depicted in the Poincaré maps. A Poincaré map is the illustration of the position and momentum coordinates of particles propagated (i.e. "tracked") through the lattice turn-by-turn, i.e. it is a phase space portrait. Figure I.9.1 shows the Poincaré maps resulting from different settings of the tune. We observe that:

- $Q_x = 0.203$ (Fig. I.9.1 top left): for a tune close to 1/5, small amplitude particles exhibit trajectories in the form of closed loops that are almost circular, i.e. indicative of the linear regime of motion. As the amplitude increases, the circular trajectories are deformed and islands become visible, in this particular case we observe *five* islands. Increasing the amplitude further, we observe regular but deformed trajectories. It even appears that for some amplitudes a large number of small islands are formed. For even higher amplitudes the trajectories become chaotic and eventually we also observe some particles getting lost (very few particle coordinates are recorded for high amplitudes as unstable particles increase in amplitude and get lost);
- $Q_x = 0.252$ (Fig. I.9.1 top right): for a tune close to 1/4 we observe a smaller region of linear motion around the origin, but already for relatively small amplitudes we see *four* islands and a strong deformation of the phase space. As before, for high amplitudes the motion becomes chaotic and eventually particles are lost;
- $Q_x = 0.33$ (Fig. I.9.1 bottom left): for a tune close to 1/3, almost all particles become unstable and rapidly increase their amplitude. Only the particle on the closed orbit (i.e. the origin of the phase space) is stable;
- $Q_x = 0.403$ (Fig. I.9.1 bottom right): adjusting the lattice to a tune close to 2/5, the phase space is more regular. We observe *five* islands, and for high amplitude particules the trajectories are regular but nevertheless deformed. In this case, for the amplitudes tested here, no unstable or chaotic motion is observed.

In summary, we have identified some interesting features in these phase space portraits to which it is worth drawing attention:

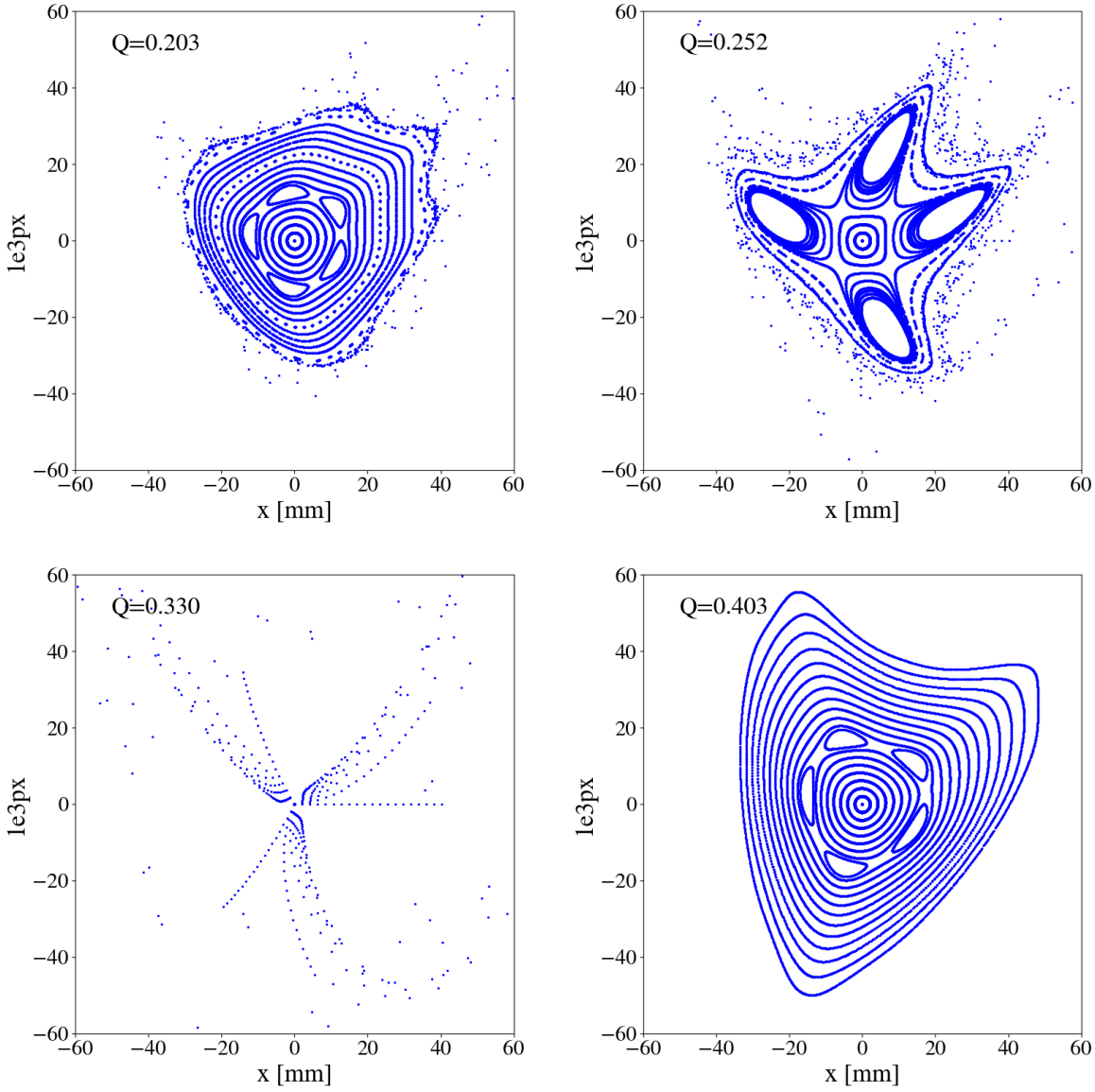

Fig. I.9.1: Poincaré maps for the simple storage ring consisting of a single sextupole magnet and a linear transport map, which is adjusted to provide a tune of $Q_x = 0.203$ (top left), $Q_x = 0.252$ (top right), $Q_x = 0.330$ (bottom left) and $Q_x = 0.403$ (bottom right).

– For small amplitudes (small x and p_x), particles trace out closed loops around the origin: this is what we expect for a purely linear map;

– As the particle amplitude is increased, "islands" appear in phase space: the phase advance (for the linear map) is often close to m/p where m is an integer and p is the number of islands;

– Sometimes, a larger number of islands appears at larger amplitude;

– Usually, there is a closed curve that divides a region of stable motion from a region of unstable motion. Outside that curve, the amplitude of particles increases without limit as the map is repeatedly applied;

– The area of the stable region depends strongly on the phase advance: for a phase advance close to $2\pi/3$, it appears that the stable region almost vanishes altogether;

– It appears that as the phase advance is increased towards π, the stable area becomes large, and distortions from the linear ellipse become less evident.

The simplified lattice is then modified to include a rotation and an octupole, and we set the tune near 1/4 (the Python code can be found in the Appendix A). Figure I.9.2 depicts the phase space (left) and the tune as a function of the initial particle amplitude (right). A "linear" detuning as a function of the oscillation amplitude is observed, which is a direct consequence of the presence of the octupole. Furthermore, the tune analysis clearly shows that particles at a specific amplitude are trapped at a tune value of $Q = 0.25$. As will be discussed in more detail later, this tune corresponds to a fourth-order resonance ($4Q_x = 1$), resulting in four resonance islands in phase space. The particles with (average) tune of $Q_x = 1/4$ are the ones inside the resonance islands.

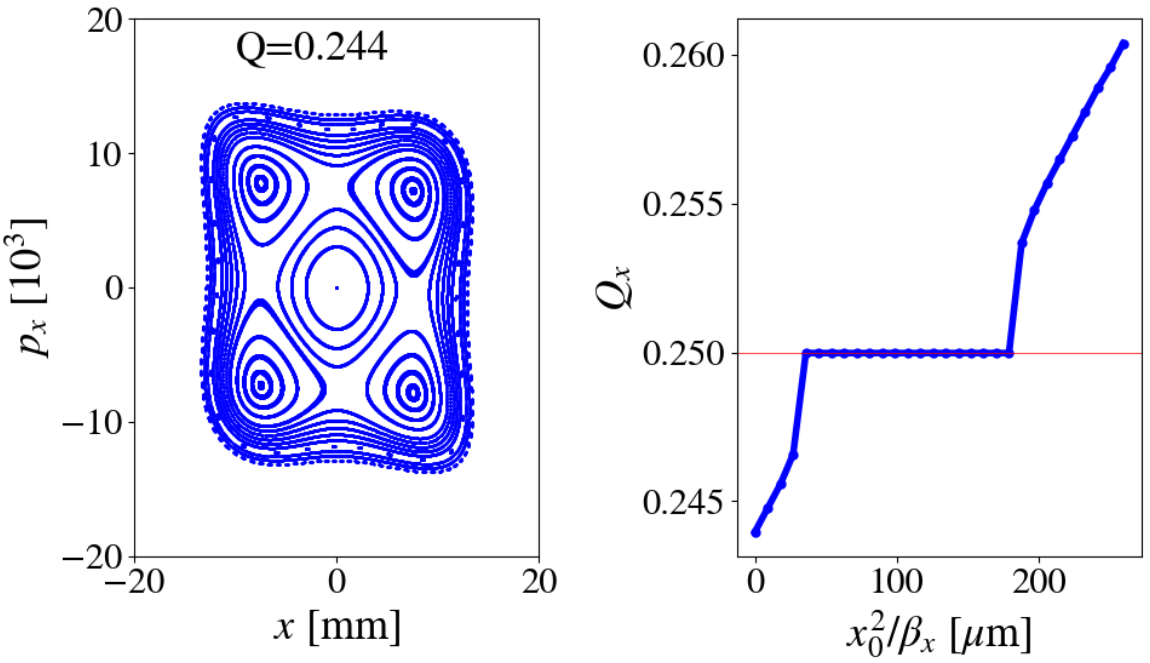

Fig. I.9.2: Phase space (left) and tune as a function of the initial particle amplitude (right) for a simple lattice consisting of a linear rotation and an octupole.

The combined effect of an octupole and sextupole is illustrated in Fig. I.9.3 and the Python code can be found in the Appendix A. Despite the tune being close to the third-order resonance (i.e. $3Q_x = 1$), particle trajectories are significantly more stable compared to the single sextupole case, cf. Fig. I.9.1 (bottom left). Some particles are captured by the stable islands of the third-order resonance, yet the majority of particles perform regular oscillations. This enhanced stability is attributed to the amplitude detuning induced by the octupole, which results in a larger distance between the high-amplitude particles and the third-order resonance and acts as a stabilizing mechanism.

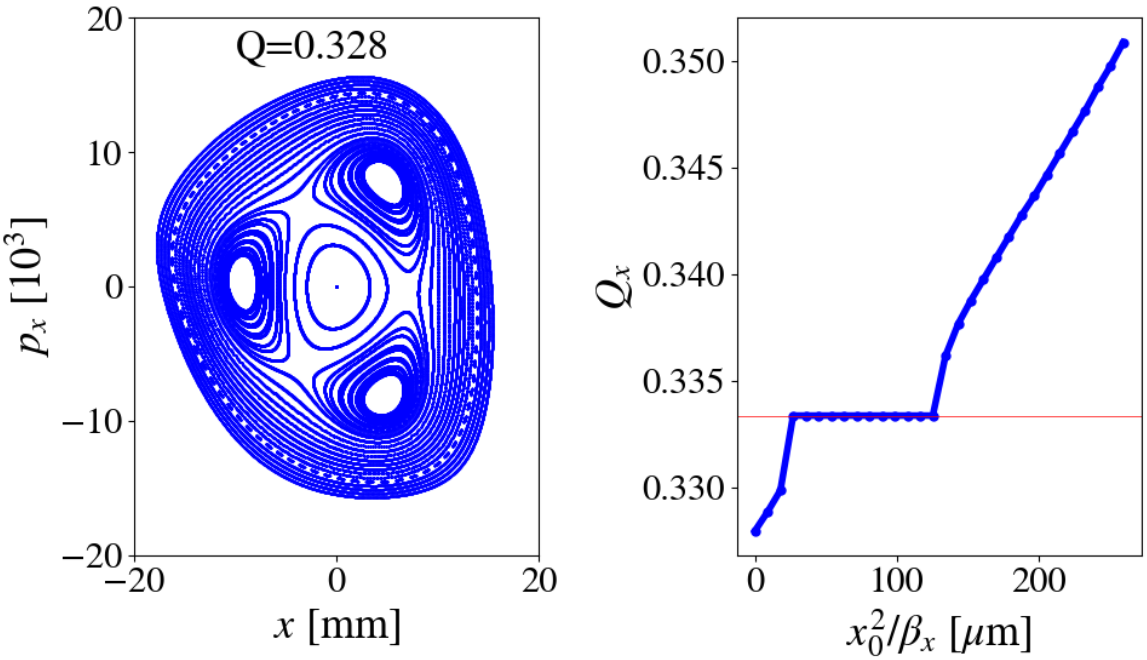

Fig. I.9.3: Phase space (left) and tune as a function of the initial particle amplitude (right) for a simple lattice consisting of a linear rotation, a sextupole and an octupole.

3 Hamiltonian mechanics

In this section we will investigate the non-linear beam dynamics from a theoretical point of view. One of the most common frameworks to describe the motion of particles in accelerators is the Hamiltonian formalism. The Hamiltonian represents the total energy of the system under study. The Hamiltonian H describing the motion of a charged particle in an accelerator can be written as

$$H = H(x_i, p_i; t), \tag{I.9.4}$$

where x_i, p_i represent the particle's position and conjugate momentum, respectively, with $i = 1, 2 \ldots N$ for the N degrees of freedom and t the time. The equations of motion are then given by Hamilton's equations

$$\frac{dx_i}{dt} = \frac{\partial H}{\partial p_i}, \tag{I.9.5}$$

$$\frac{dp_i}{dt} = -\frac{\partial H}{\partial x_i}. \tag{I.9.6}$$

Considering only horizontal motion (x, p_x) to simplify the analysis, the time derivative of the Hamiltonian can be expressed as

$$\frac{dH}{dt} = \frac{\partial H}{\partial x}\frac{dx}{dt} + \frac{\partial H}{\partial p_x}\frac{dp_x}{dt} + \frac{\partial H}{\partial t}. \tag{I.9.7}$$

By differentiating the Hamiltonian with respect to position or momentum, we obtain Hamilton's

equations. Using Hamilton's equations we find that

$$\frac{dH}{dt} = \frac{\partial H}{\partial x}\frac{\partial H}{\partial p_x} - \frac{\partial H}{\partial p_x}\frac{\partial H}{\partial x} + \frac{\partial H}{\partial t} = \frac{\partial H}{\partial t}, \tag{I.9.8}$$

i.e., if the Hamiltonian does not depend explicitly on the time t, the Hamiltonian is conserved since

$$\frac{dH}{dt} = \frac{\partial H}{\partial t} = 0. \tag{I.9.9}$$

Hamiltonian systems are inherently symplectic, meaning that the phase space structure is preserved. Additionally, Eq. I.9.9 shows that in the absence of external time-dependent forces or dissipative effects such as synchrotron radiation, the Hamiltonian remains constant and is an *integral* of motion. A consequence of this is that the phase space volume is preserved, which is known as the *Liouville's theorem*. In practice, Liouville's theorem implies that, under these assumptions, quantities such as the emittance of a beam remain constant over time.

3.1 Hamiltonian for linear betatron motion

The Hamiltonian for linear betatron motion in a lattice with dipoles and quadrupoles is given as a function of the azimuthal coordinate s by

$$H(s) = \frac{\bar{p}_x^2 + \bar{p}_y^2}{2} - \frac{x^2}{2\rho(s)^2} + \frac{k_1(s)}{2}(x^2 - y^2), \tag{I.9.10}$$

where $\frac{\bar{p}_x^2+\bar{p}_y^2}{2}$ is the kinetic term and $\bar{p}_x = \frac{p_x}{p_0}$ and $\bar{p}_y = \frac{p_y}{p_0}$ are the transverse momenta normalized to the reference momentum p_0, $\frac{x^2}{2\rho(s)^2}$ is the weak focusing from the dipoles with a bending radius $\rho(s)$, and $\frac{k_1(s)}{2}(x^2 - y^2)$ is the focusing (or defocusing depending on the sign) of the quadrupoles' strength $k_1(s)$.

Applying Hamilton's equations (cf. Eq. I.9.5) we derive the equations of motion for a linear accelerator, known as Hill's equations

$$x'' - \left(\frac{k_1(s) - 1}{\rho(s)^2}\right) x = 0, \tag{I.9.11}$$

$$y'' + k_1(s)y = 0, \tag{I.9.12}$$

where x'' and y'' are the second derivatives of the horizontal and vertical coordinates with respect to the longitudinal position s.

3.2 Hamiltonian with nonlinear fields

The dynamics of the particle motion in a more realistic accelerator lattice cannot be described by the linear Hamiltonian due to the presence of higher-order multipoles. Nonlinear fields play an important role in accelerator operation, for example for chromaticity control, or to suppress coherent motion. Nonlinear fields also arise naturally from the interaction of two colliding beams.

The general Hamiltonian for a charged particle in an accelerator with transverse magnetic fields can be written as

$$H(s) = \frac{\bar{p}_x^2 + \bar{p}_y^2}{2} - \frac{eA_s}{p_0}, \tag{I.9.13}$$

where e is the elementary charge and A_s is the longitudinal component of the magnetic vector potential. Here we consider only purely transverse magnetic fields, i.e. we apply the hard edge approximation in which the magnetic fields are assumed to vanish outside of the magnets and the components of the magnetic field are given by

$$B_x = \frac{\partial A_s}{\partial y}, \quad B_y = -\frac{\partial A_s}{\partial x}. \tag{I.9.14}$$

It is convenient and customary to use a complex representation of the magnetic field such as

$$B_y + iB_x = B_0 p_0 \sum_{n=0}^{M} (k_n + ij_n) \frac{(x+iy)^n}{n!}, \tag{I.9.15}$$

where B_0 is the reference magnetic field and k_n, j_n are the normal and skew multipole strengths, respectively, given by

$$k_n = \frac{1}{B_0 p_0} \left. \frac{\partial^n B_y}{\partial x^n} \right|_{(0,0)}, \tag{I.9.16}$$

$$j_n = \frac{1}{B_0 p_0} \left. \frac{\partial^n B_x}{\partial y^n} \right|_{(0,0)}. \tag{I.9.17}$$

The subscript $(0,0)$ indicates that the n-th partial derivatives are computed for (x, y)=(0,0), i.e. on the design trajectory of the accelerator. The magnetic potential can thus be expressed by the following multipole expansion

$$\frac{eA_s}{p_0} = \frac{x^2}{2\rho^2} - \text{Re}\left\{ \sum_{n=1}^{M} \frac{(k_n + ij_n)(x+iy)^{n+1}}{(n+1)!} \right\}. \tag{I.9.18}$$

The Hamiltonian in the presence of nonlinear fields is then obtained as

$$H(s) = \frac{\bar{p}_x^2 + \bar{p}_y^2}{2} - \frac{x^2}{2\rho^2} + \text{Re}\left\{ \sum_{n=1}^{M} \frac{(k_n + ij_n)(x+iy)^{n+1}}{(n+1)!} \right\}, \tag{I.9.19}$$

and it can be divided in a linear part H_0 including dipole and quadrupole fields

$$H_0(s) = \frac{\bar{p}_x^2 + \bar{p}_y^2}{2} - \frac{x^2}{2\rho(s)^2} + \frac{k_1(s)}{2}(x^2 - y^2) \tag{I.9.20}$$

and a nonlinear part that containes the nonlinear multipole field components

$$V(s) = \text{Re}\left\{ \sum_{n\geq 2} \frac{[k_n(s) + ij_n(s)](x+iy)^{n+1}}{(n+1)!} \right\} = \sum_{m,n\geq 3} V_{mn} x^m y^n. \tag{I.9.21}$$

3.3 Action-angle variables

The linear part of the Hamiltonian can be reduced to a simple rotation with a canonical transformation, i.e. a change of variables that preserves Hamilton's equations. This transformation converts the particle's phase space from the coordinates (x, p_x) to the *action-angle variables* (J, φ). The action variable J

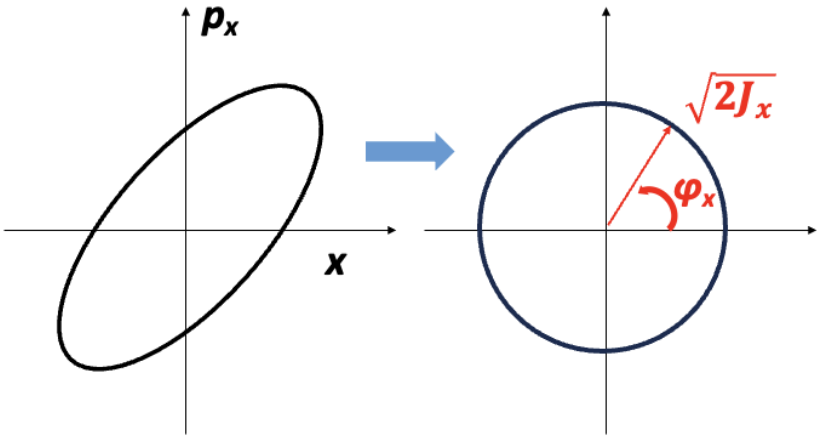

Fig. I.9.4: The evolution of phase space from ellipses (left) to circles (right) via the canonical transformation to action-angle variables.

corresponds to the Courant-Snyder invariant for the linear motion

$$J_x = \gamma_x x^2 + 2\alpha_x x p_x + \beta_x p_x^2, \tag{I.9.22}$$

while the angle variable is

$$\varphi_x = -\arctan\left(\frac{\beta_x p_x}{x} + \alpha_x\right). \tag{I.9.23}$$

By moving to action-angle variables, the particle's motion in phase space is transformed from an ellipse to a simple rotation on a circle with a radius equal to $\sqrt{2J_x}$, as shown in Fig. I.9.4, and with an angle change per turn equal to $\Delta\varphi_x = 2\pi Q_{x0}$, where Q_{x0} is the betatron tune.

In systems with more degrees of freedom, the particle trajectories are a product of circles (u, p_u) with action-angle variables J_u and φ_u that are forming multi-dimensional *tori*. As will be shown in the next sections, when a nonlinearity is introduced, resulting in a change of p_u, the tori will be distorted and, in the presence of a strong nonlinearity, some tori might even be destroyed.

4 Resonance driving terms and resonances

The Hamiltonian in action-angle variables is obtained as

$$H(\mathbf{J}, \boldsymbol{\varphi}; s) = \frac{Q_x J_x + Q_y J_y}{R} + V(\mathbf{J}, \boldsymbol{\varphi}; s), \tag{I.9.24}$$

where Q_x, Q_y are the horizontal and vertical tunes and R is the (average) radius of the accelerator. In perturbation theory, the nonlinear part of the Hamiltonian V can be written as

$$V(\mathbf{J}, \boldsymbol{\varphi}; s) = \frac{\varepsilon}{R} \sum_{\substack{j=0 \\ j+k=m_x}}^{m_x} \sum_{\substack{l=0 \\ l+m=m_y}}^{m_y} (J_x^{\frac{j+k}{2}} J_y^{\frac{l+m}{2}} h_{jklm} e^{i[(j-k)\varphi_x + (l-m)\varphi_y]}), \tag{I.9.25}$$

where ε is the parameter that controls the strength of the perturbation, m_x, m_y are integers that define the order of the *resonance* and the complex coefficients h_{jklm} are known as the *resonance driving terms*. These terms are responsible for angle-dependent terms in the Hamiltonian that can lead to resonant motion, such as motion on islands or on a separatrix in phase space. The resonance driving terms are determined by integrals over the circumference of the accelerator that depend on the location of the multipolar magnetic elements

$$h_{jklm} = \frac{1}{2^{\frac{j+k+l+m}{2}}} \left(\frac{j+k}{j}\right) \left(\frac{l+m}{l}\right) \int_{s_0}^{s_0+2\pi R} V_{j+k,l+m}(s) \beta_x^{\frac{j+k}{2}}(s) \beta_y^{\frac{l+m}{2}}(s) e^{i[(j-k)\varphi_x(s)+(l-m)\varphi_y(s)]}\, ds. \quad \text{(I.9.26)}$$

To first order of the multipole strengths, the solution for the stable betatron motion can be written as a *quasi-periodic* solution, i.e. a sum of periodic motions with different frequencies

$$x(n) - ip_x(n) = \sqrt{2J_x} e^{i(2\pi Q_x n + \varphi_{x0})} - 2i \sum_{jklm} s_{jklm} \left(2J_x\right)^{\frac{j+k-1}{2}} \left(2J_y\right)^{\frac{l+m}{2}} e^{i[(1-j+k)(2\pi Q_x n+\varphi_{x0})+(m-l)(2\pi Q_y n+\varphi_{y0})]}, \quad \text{(I.9.27)}$$

where

$$s_{jklm} = \frac{1}{1 - e^{-2\pi i[(j-k)Q_x+(l-m)Q_y]}} h_{jklm}. \quad \text{(I.9.28)}$$

The stable solutions of the betatron motion include the resonance driving terms, and the resonance conditions are defined by the integer multiples of the betatron tunes Q_x and Q_y. A resonance can occur when

$$n_x Q_x + n_y Q_y = r, \quad \text{(I.9.29)}$$

where $n_x = j - k$, $n_y = l - m$ and $|n_x|+|n_y|$ is the resonance order. In the space of the horizontal and vertical tunes, namely the *tune diagram*, the resonance conditions of Eq. I.9.29 are depicted as lines. Figure I.9.5 illustrates the resonance condition for the resonances up to third (left) and fifth (right) order. Skew resonances (excited by skew multipole components), for which n_y is an odd number, are represented by dashed lines. Normal resonances (excited by upright multipole components), characterized by an even n_y, are marked with solid lines. A summary of the resonance driving terms and resonance conditions is shown in Table I.9.1.

Indices	j, k, l, m
Resonance Driving Term	h_{jklm}
Potential	$V_{j+k,l+m}$
Resonance condition	$(j-k)Q_x + (l-m)Q_y = r$
Resonance order	$\lvert j-k\rvert + \lvert l-m\rvert$

Table I.9.1: Summary of resonance driving terms and resonance conditions.

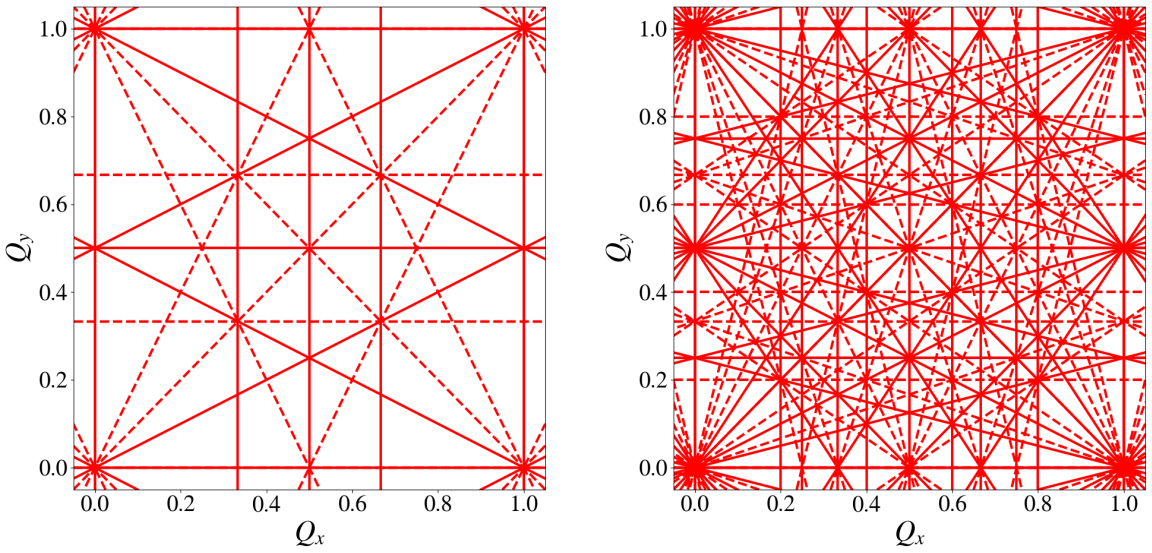

Fig. I.9.5: Resonances within the tune diagram up to the third (left) and fifth (right) order. Normal (solid lines) and skew (dashed lines) resonances are illustrated.

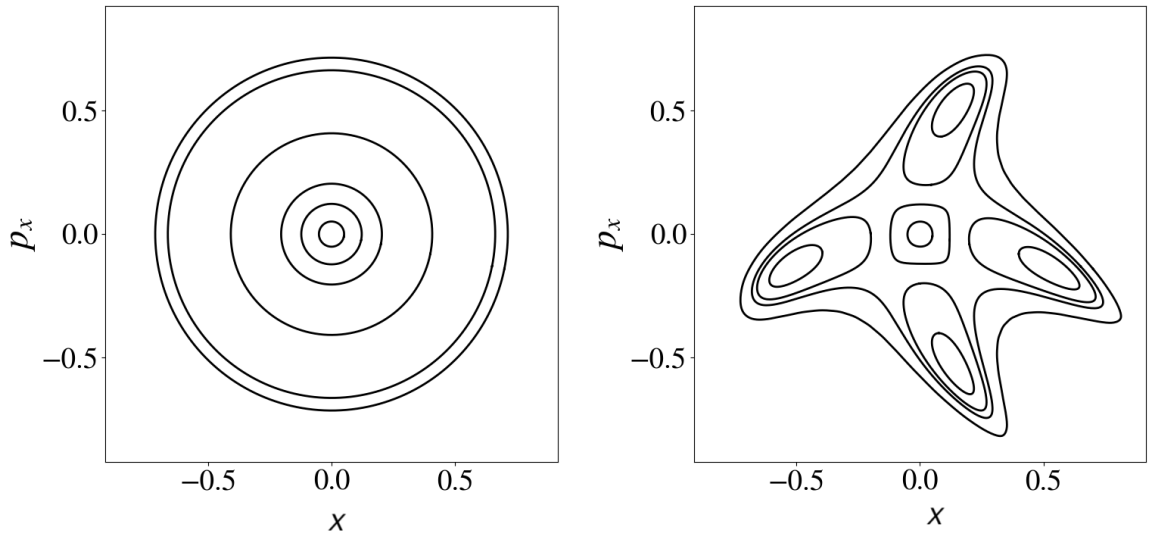

Fig. I.9.6: Phase space in the presence of angle-independent resonance driving terms (left) that result in amplitude detuning and angle-dependent (right) resonance driving terms responsible for the formation of resonance islands. Courtesy of P. Bélanger.

A review of Eq. I.9.25 reveals two types of resonance driving terms, and their impact on the particle's phase space is illustrated in Fig. I.9.6:

– Angle-*independent* resonance driving terms (Fig. I.9.6, left): for $j = k$ and $l = m$ and the lowest order in the multipolar gradient, the exponential factor is equal to one and the dependence on the angle vanishes. The nonlinear part of the Hamiltonian depends only on the particle action resulting

in a detuning with amplitude and has the form of

$$V(\mathbf{J},\boldsymbol{\varphi};s)=\frac{\varepsilon}{R}\sum_{\substack{j=0\\2j=m_x}}^{m_x}\sum_{\substack{l=0\\2l=m_y}}^{m_y}J_x^jJ_y^lh_{jjll}. \tag{I.9.30}$$

– Angle-*dependent* resonance driving terms (Fig. I.9.6, right): these terms are responsible for the excitation of resonances by creating fixed point and island structures in phase space. For example, for the fourth order resonance (4,0)

$$V(\mathbf{J},\boldsymbol{\varphi};s)=\frac{\varepsilon}{R}J_x^2h_{4000}e^{i4\varphi_x}. \tag{I.9.31}$$

4.1 Sextupole driving terms in first-order perturbation theory

The sextupole driving terms are calculated by substituting the magnetic potential in Eq. I.9.26 by

$$V(s)=b_2(s)(x^3-3xy^2)=V_{30}(s)x^3-V_{12}(s)xy^2, \tag{I.9.32}$$

where b_2 is the sextupole strength at the position s and V_{30}, V_{12} are the $V_{j+k,l+m}(s)$ with $j+k$=3, $l+m$=0 and $j+k$=1, $l+m$=2, respectively, that excite the following resonances $(j-k)Q_x+(l-m)Q_y$:

– V_{30}: h_{3000}, h_{2100} for the purely horizontal resonances (3,0), (1,0);

– V_{12}: h_{1011}, h_{1020}, h_{1002} and resonances (1,0), (1,2), (1,-2).

In first-order of the sextupole strengths, sextupoles are driving integer and third-order resonances, they are exciting purely horizontal resonances (but not purely vertical ones) and coupled resonances, while amplitude detuning $j=k, l=m$ is not generated (amplitude detuning is only generated in second order of the sextupole strength).

The topology of the third-order horizontal resonance is shown in Fig. I.9.7. Near the origin of the phase space, the motion of particles is regular and follows nearly circular paths. As the amplitude of particle oscillations increases, these trajectories become distorted, tending towards a triangular shape, a signature of third-order resonances. The boundary between stable and unbounded motion is referred to as *separatrix* and it connects the three unstable (hyperbolic) fixed points, which are points in phase space where particles will jump on one side of separatrix for tiniest perturbations.

4.2 Octupole driving terms in first-order perturbation theory

The octupole driving terms are calculated by substituting the magnetic potential in Eq. I.9.26 by

$$V(s)=b_3(s)(x^4-6x^2y^2+y^4)=V_{40}(s)x^4+V_{22}(s)x^2y^2+V_{04}(s)y^4, \tag{I.9.33}$$

where b_3 is the octupole strength and V_{40}, V_{22} and V_{04} are the $V_{j+k,l+m}$ with $j+k$=4, $l+m$=0, then $j+k$=2, $l+m$=2 and finally, $j+k$=0, $l+m$=4. The excited resonance driving terms and the resonances $(j-k)Q_x+(l-m)Q_y$ are:

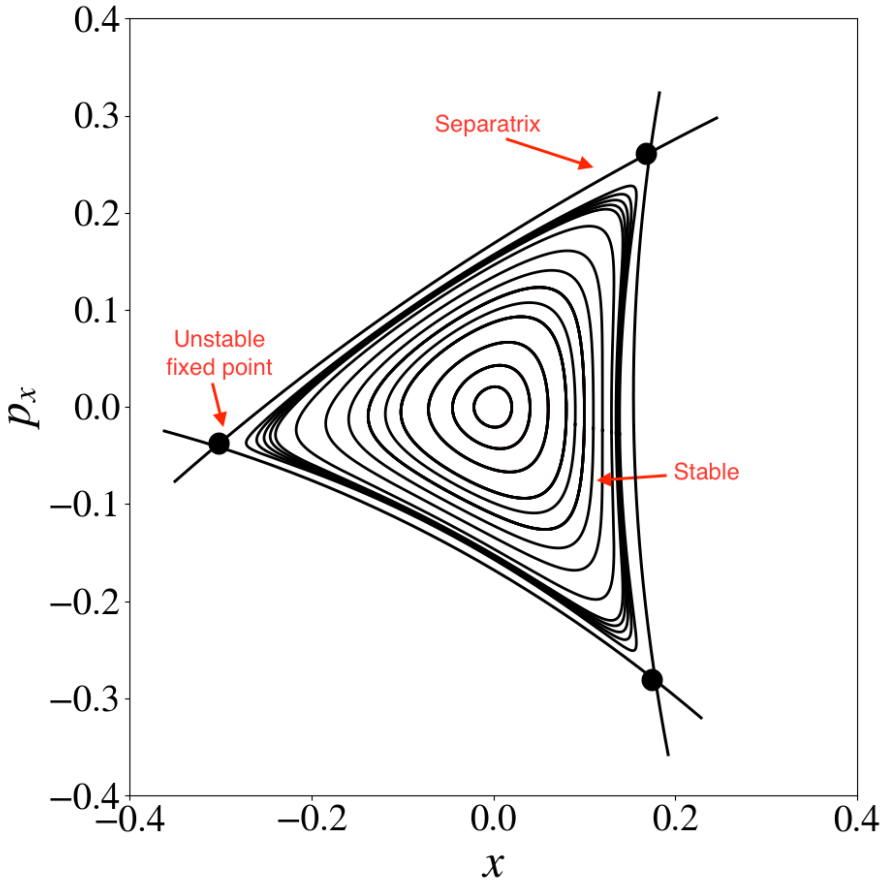

Fig. I.9.7: Phase space in the vicinity of the third-order resonance. Courtesy of P. Bélanger.

– V_{40}: h_{4000}, h_{3100}, h_{2200}, resonances (4,0), (2,0) and an angle-independent resonance driving term ($j = k = 2, l = m = 0$) that introduces detuning with amplitude;

– V_{22}: h_{2020}, h_{1120}, h_{2011}, h_{1111}, resonances (2,2), (0,2), (2,0) and an amplitude detuning resonance driving term ($j = k = 1, l = m = 1$);

– V_{04}: h_{0040}, h_{0031}, h_{0022}, resonances (0,4), (0,2) and an amplitude detuning resonance driving term ($j = k = 0, l = m = 2$).

Octupoles introduce amplitude detuning, excite second and fourth order resonances in first-order perturbation theory and they also excite both purely horizontal but also purely vertical resonances.

Figure I.9.8 illustrates the topology of the fourth-order resonance. Near the origin of the phase space, the motion is regular. The trajectories in phase space tend towards a square shape. The separatrix connects four unstable fixed points. There are also four stable fixed points. These are points where the motion is stable, and they are surrounded by closed, regular trajectories, forming islands of stability in phase space.

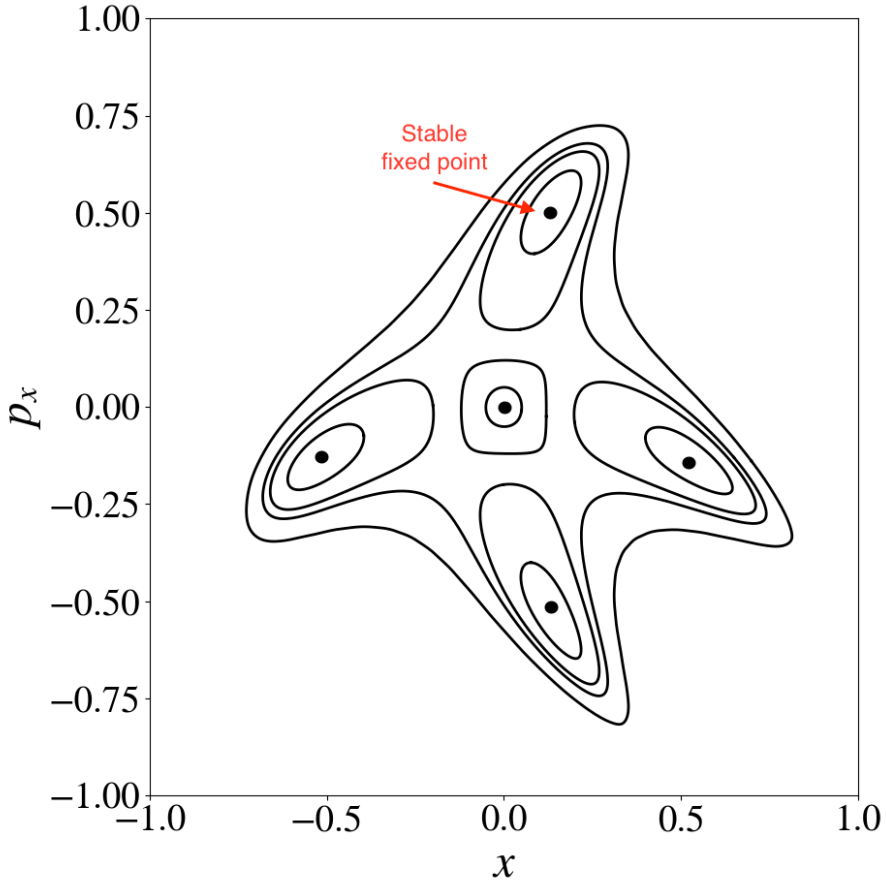

Fig. I.9.8: Phase space in the vicinity of the fourth-order resonance. Courtesy of P. Bélanger.

4.3 Sextupole resonances in second-order perturbation theory

The Hill's equation can be modified to include the sextupole term k_2

$$\frac{d^2x}{ds^2} + K(s)x = \frac{k_2}{2}x^2, \tag{I.9.34}$$

where $K(s)$ represents the linear part

$$K(s) = \frac{1}{\rho^2(s)} - k_1(s). \tag{I.9.35}$$

The solution to Hill's equation can be written as a series expansion with a small perturbation ε due to the sextupole which is proportional to k_2. The solution will have the form

$$x(s) = x_0 + \varepsilon x_1(s) + \varepsilon^2 x_2(s) + O(\varepsilon^3), \tag{I.9.36}$$

with x_0 representing the solution of the unperturbed linear equation and x_1 and x_2 the first and second-order perturbation from the sextupoles, respectively, while $O(\varepsilon^3)$ represents the higher-order terms. By inserting the series expansion of Eq. I.9.36 into Eq. I.9.34 and matching terms of the same order in ε, the

following equations are derived

$$\frac{d^2x_0}{ds^2} + K(s)x_0 = 0, \tag{I.9.37}$$

$$\frac{d^2x_1}{ds^2} + K(s)x_1 = k_2(s)x_0^2(s), \tag{I.9.38}$$

$$\frac{d^2x_2}{ds^2} + K(s)x_2 = 2k_2(s)x_0(s)x_1(s). \tag{I.9.39}$$

Starting from the linear solution

$$x_0(s) = \sqrt{\varepsilon_x\beta_x(s)}\cos[\varphi_x(s) + \varphi_{x0}], \tag{I.9.40}$$

where φ_{x0} is the initial phase of the particle and computing sequentially the other terms, using the solutions from previous steps to calculate the next one we obtain

$$x_1(s) \propto A\cos[2\varphi_x(s) + \varphi_{x0}], \tag{I.9.41}$$

$$x_2(s) \propto C\cos[3\varphi_x(s) + \varphi_{x0}] + D\cos[\varphi_x(s) + \varphi_{x0}]. \tag{I.9.42}$$

As was shown in the previous section, in first-order perturbation theory the phase $2\varphi_x$ of x_1 results in the excitation of third-order resonances. Similarly, in the second-order of the sextupole strengths, the phase $3\varphi_x(s)$ and $\varphi_x(s)$ in the solution x_2 indicate that the sextupoles are capable of exciting fourth-order and second-order resonances. In practice, sextupoles can excite resonances up to very high orders, as we have observed in Fig. I.9.1 (e.g. fifth order resonances).

5 Chaos

5.1 KAM theorem and onset of chaos

The Kolmogorov-Arnold-Moser (KAM) theorem describes the behavior of Hamiltonian systems when subjected to small perturbations. In an integrable system, phase space motion can be represented by invariant tori, where motion is regular, predictable and quasi-periodic. According to the KAM theorem, with the introduction of small perturbations, many of these invariant tori are deformed but still survive so that particle motion remains confined and stable within these tori.

However, as the strength of the nonlinearity increases or the system approaches a resonance condition, some invariant tori are destroyed. When this happens, trajectories that were once confined to the surface of the torus can now have irregular, unpredictable or chaotic behavior.

As perturbations increase, the motion around the unstable fixed points also becomes more complex. Initially, some trajectories near these points may follow predictable paths, but as the system is perturbed, these paths can start to intertwine and form complex structures known as *tangles* as shown in Fig. I.9.9. Tangles are intersections of stable and unstable paths from and to unstable fixed points and they represent complex trajectory structures. They introduce a sensitivity to initial conditions as particles with slightly different starting points crossing these tangles can have vastly different paths. As shown in the phase space illustrated in Fig. I.9.10, the motion around the separatrix becomes chaotic.

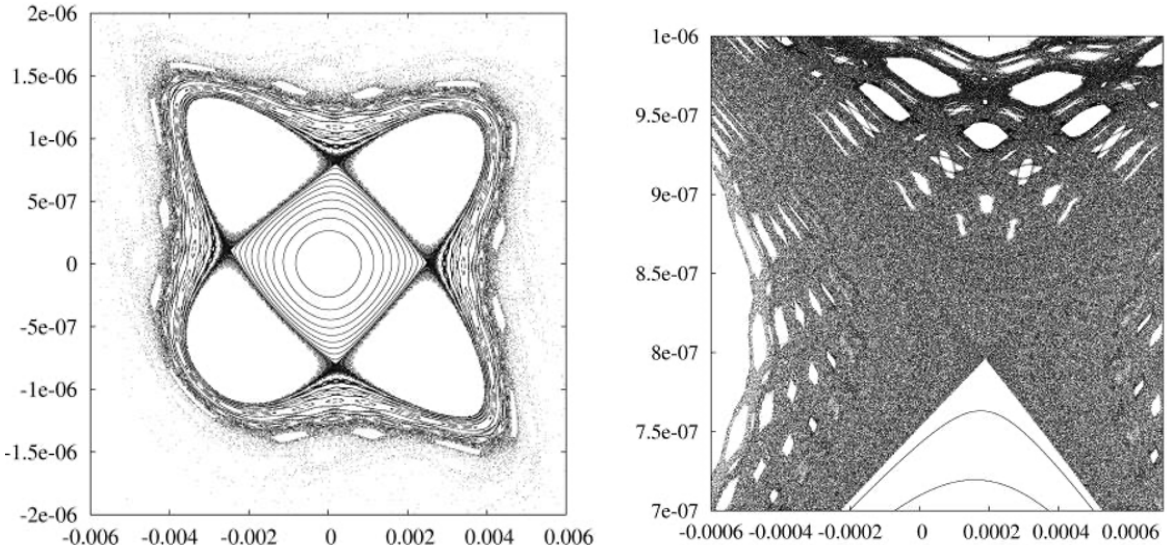

Fig. I.9.9: Formation of tangles around the unstable fixed points of a fourth order resonance.

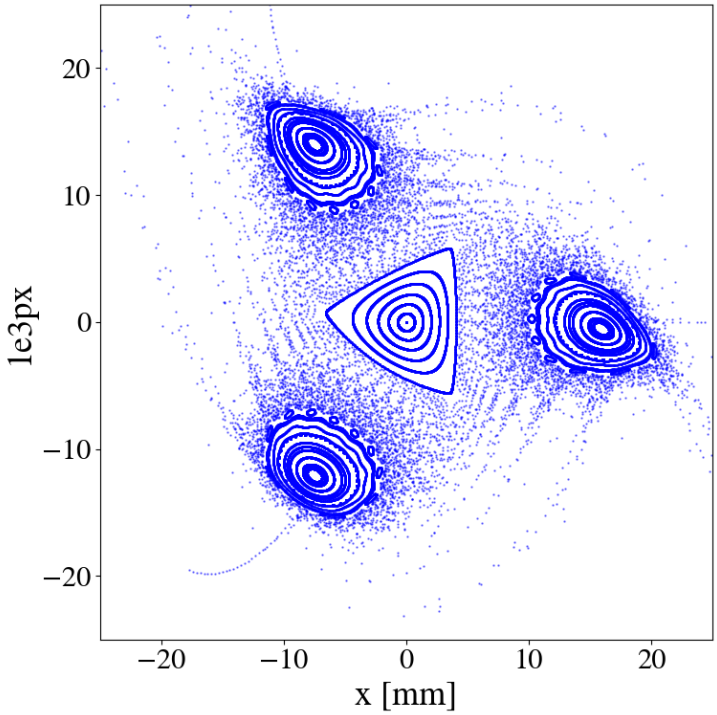

Fig. I.9.10: Chaotic motion around the separatrix due to strong nonlinear perturbations.

5.2 Resonance overlap

With increasing perturbation, the width of the resonance islands in the phase space grow. Although islands are regions of stable motion, when they start overlapping the particle can move from one island to the other, facilitating chaotic motion across the phase space. This condition, known as *resonance overlap criterion*, was described by B. Chirikov [14]. The Chirikov criterion states that chaos emerges when the sum of the half-widths J of two resonances of order k and k' exceeds the distance between

them

$$\Delta\hat{J}_{k\max} + \Delta\hat{J}_{k'\max} \geq \delta\hat{J}_{k,k'}. \tag{I.9.43}$$

A rule of thumb is that significant chaos is expected when the sum of the maximum widths of the chaotic layers around two resonances is greater than two-thirds of the distance between the resonances

$$\Delta\hat{J}_{k\max} + \Delta\hat{J}_{k'\max} \geq \frac{2}{3}\delta\hat{J}_{k,k'}. \tag{I.9.44}$$

The resonance overlap is illustrated in Figure I.9.11. Increasing the strength of the nonlinearity (left to right), the width of the resonances increases and eventually the islands overlap leading to chaotic motion. The main limitation of this criterion is its geometrical nature, which makes it difficult to apply for systems with more degrees of freedom.

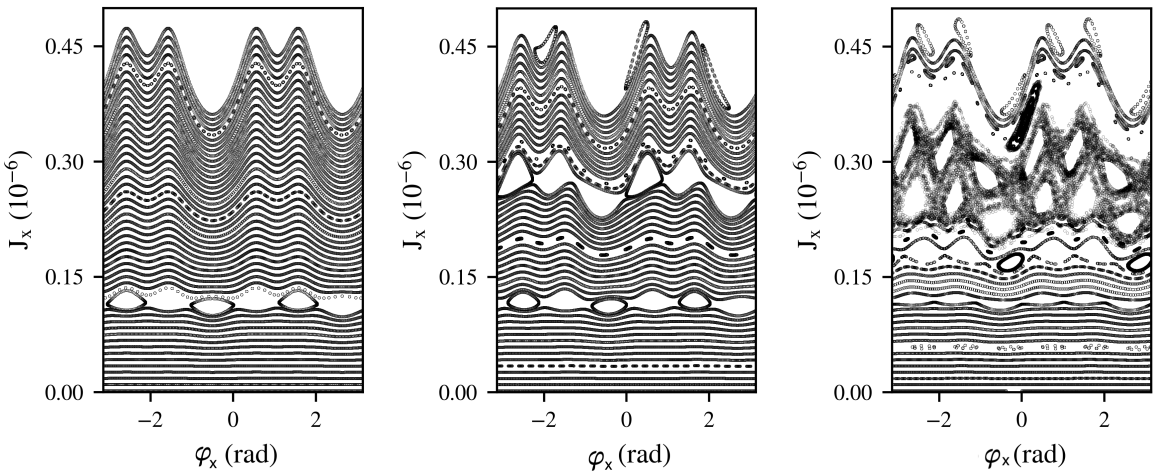

Fig. I.9.11: The impact of resonance overlap when increasing the strength of a perturbation (left to right).

6 Resonance compensation

The excitation of resonances due to nonlinear fields is a significant contributor to unstable particle motion, particle losses and emittance growth. These issues undermine the performance of an accelerator, as they can limit the achievable beam intensity and beam emittances. Despite these undesirable effects, nonlinear magnets are crucial for the operation of the accelerator as they allow fine tuning of the beam dynamics such as the correction of chromaticity with sextupoles and inducing amplitude detuning with octupoles to Landau damp coherent instabilities. Additionally, certain nonlinear effects are unavoidable as they are an inherent consequence of magnet imperfections or result from the interplay between the colliding beams (beam-beam effects).

There are several strategies to mitigate the adverse effects of resonances. One approach involves the strategic design of the accelerator's lattice with a specific periodicity, which means that the accelerator is structured in repetitive cells and the lattice symmetry allows to minimize or even cancel some resonance driving terms. Another approach involves the use of specialized magnets to correct for specific resonance driving terms.

6.1 Lattice periodicity

Considering a lattice with tunes Q_x and Q_y and P identical cells, the phase advance per cell is Q_x/P and Q_y/P. Since for the beam there is no difference between passing one cell P turns or passing a lattice consisting of P identical cells only once, the resonance condition must be satisfied by each individual cell. Thus the resonance condition of Eq. I.9.29 within a cell takes the following form

$$n_x \frac{Q_x}{P} + n_y \frac{Q_y}{P} = \frac{r}{P}. \tag{I.9.45}$$

Based on the lattice periodicity, the resonances can be divided into two categories:

- Systematic resonances arise when $\frac{r}{P}$ is an integer. In this case, the perturbation from the nonlinear magnetic fields at each cell will accumulate systematically cell-by-cell. Such resonances arise from the lattice design and structure.

- When $\frac{r}{P}$ is not an integer, the resonance is non-systematic. As the particle passes through the cells it will experience a varying perturbation cell by cell and the cumulative impact of the resonance is, to first-order, cancelled. This cancellation requires a perfectly periodic lattice, a condition that easily breaks in the presence of random magnet errors.

Figure I.9.12 depicts the tune diagram up to fourth order resonances for a lattice with periodicity $P = 1$ (top left), $P = 2$ (top right) and $P = 3$ (bottom). The systematic resonances are illustrated in red, and the non-systematic ones in blue. Obviously, the higher the lattice periodicity the more resonances become non-systematic, i.e. suppressed by the lattice symmetry.

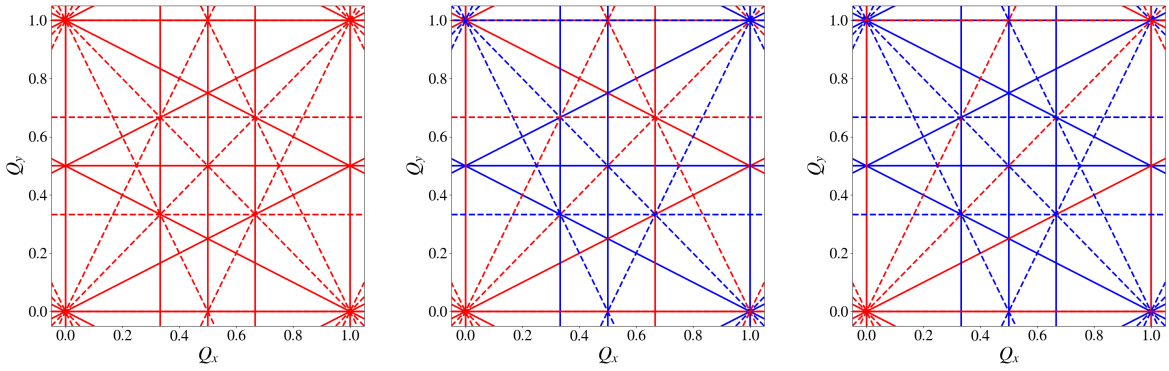

Fig. I.9.12: Tune diagram up to the fourth order for a lattice with periodicity $P = 1$ (left), $P = 2$ (center) and $P = 3$ (right). The systematic resonances are illustrated in red, and the non-systematic ones in blue.

Non-systematic resonances can be corrected (to first-order) by having a good control of the lattice's symmetry. The correction of the non-systematic resonances was demonstrated at the Advanced Light Source (ALS) at Lawrence Berkeley National Laboratory [15]. The ALS nominal lattice has a periodicity of $P = 12$. Thus, the third order resonance $3Q_x = 43$ is non-systematic (ratio 43/12 is not an integer) and the fifth order resonance $5Q_x = 72$ is systematic (ratio 72/12 is an integer). The beam loss rate was measured when the horizontal tune was changed to cross these two resonances as shown in Fig. I.9.13. Initially, important losses were observed when crossing both resonances (dashed line) when the linear

optics was uncorrected and the β-beating was around 30%. The measurement was repeated after optics corrections that effectively reduced β-beating to around 1%, restoring the lattice's periodicity to $P = 12$ (dashed line). The impact from the non-systematic resonance $3Q_x = 43$ was suppressed, while the losses around the systematic resonance $5Q_x = 72$ were unaffected.

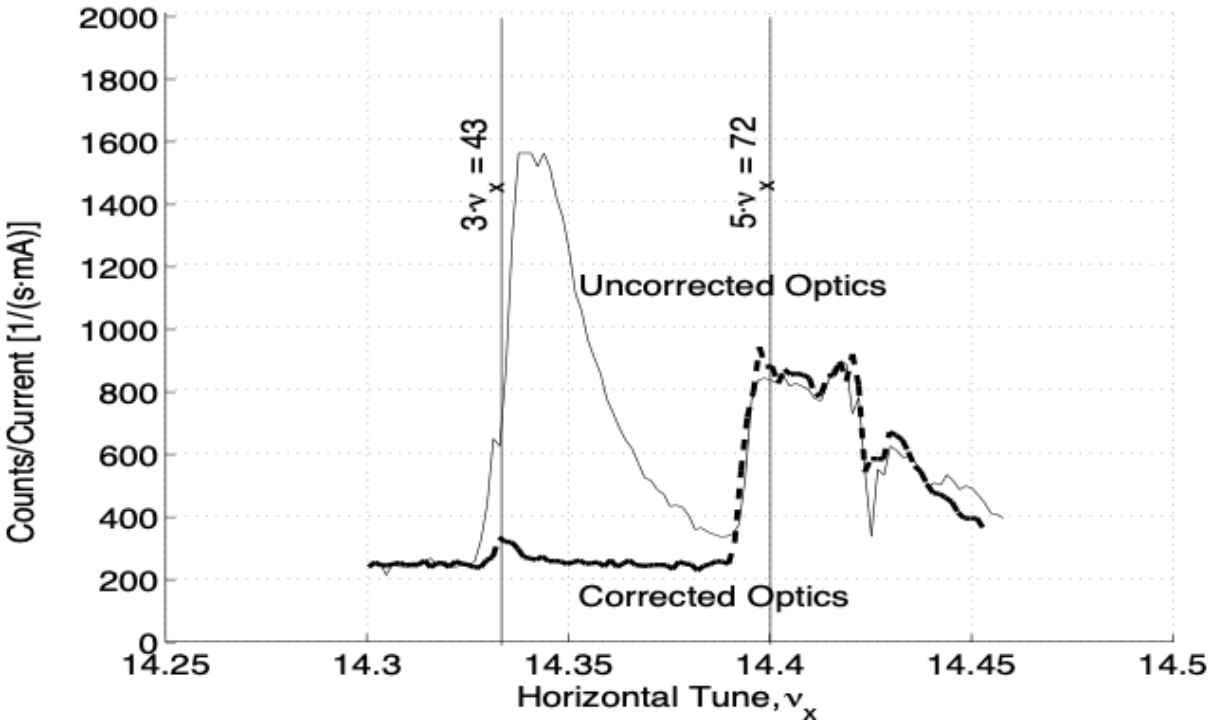

Fig. I.9.13: Beam loss rate when crossing a non systematic $3Q_x = 43$ resonance and a systematic $5Q_x = 72$ resonance in ALS with $P = 12$ before (solid line) and after (dashed line) optics corrections that restored the lattice periodicity [15].

6.2 Resonance driving term compensation with correctors

Mitigating weak resonances (e.g. non-systematic resonancs excited by random magnet errors in the machine) can also be achieved by using a pair of multipole correctors that are approximately orthogonal in the phase of the resonance driving terms. Such correctors are ideally installed in low-dispersion regions to avoid influencing the chromaticity. It must be noted that although these correctors are adjusted to compensate for a specific resonance, they might also excite other resonances.

The Proton Synchrotron Booster (PSB) at CERN employs a stack of multipole correctors, including quadrupoles, sextupoles, and octupoles (both normal and skew), to compensate for various resonances [16]. The resonance compensation is necessary due to the large tune spread caused by space charge effects. Figure I.9.14 illustrates the loss maps, which are computed by scanning the horizontal and vertical tunes and measuring the losses. A comparison before (left) and after (right) the resonance compensation clearly shows the reduction of the resonance strengths.

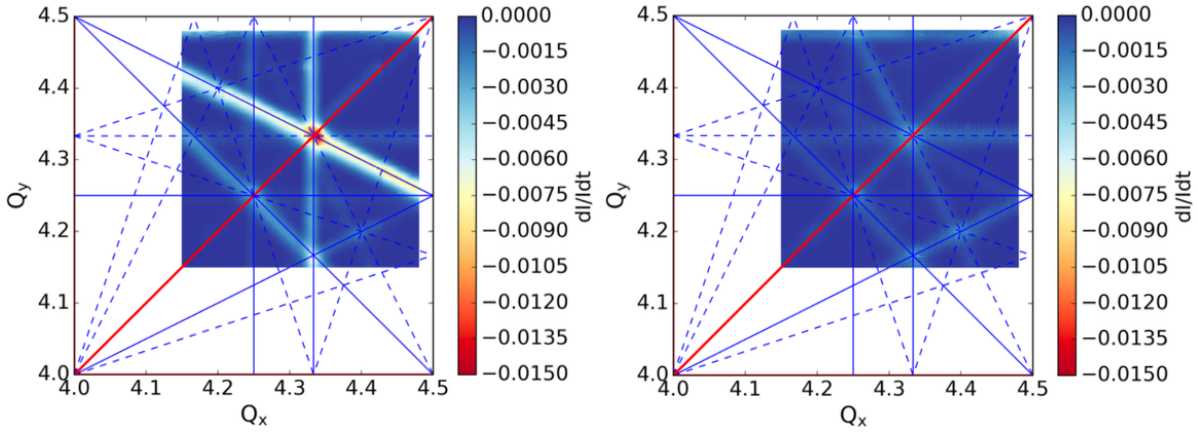

Fig. I.9.14: Tune loss maps in the PSB before (left) and after (right) the resonance compensation [16].

7 Transfer maps

7.1 Taylor maps

The evolution of the particle's coordinates when passing through an accelerator (or part of it) can be represented by transfer maps. In particular, the evolution of x_j, representing any of the six phase space coordinates $(x, p_x, y, p_y, z, \delta)$, can be expressed as a series expansion that includes terms up to a specific order, which is known as Taylor map. For example, the evolution of x_j to its final state x_j^f calculated by a third order Taylor map is written as

$$x_j^f = \sum_{k=1}^{6} R_{j,k} x_k + \sum_{k=1}^{6}\sum_{l=1}^{6} T_{j,k,l} x_k x_l + \sum_{k=1}^{6}\sum_{l=1}^{6}\sum_{m=1}^{6} U_{j,k,l,m} x_k x_l x_m, \tag{I.9.46}$$

where $R_{j,k}$, $T_{j,k,l}$, $U_{j,k,l,m}$ are the linear, quadratic and cubic coefficients, respectively.

The main drawback of this approach is that truncated Taylor maps (i.e. Taylor maps including terms up to a finite number of terms) are in many cases not symplectic (unless special terms are included to ensure symplecticity). This leads to inaccuracies in the simulation of particle dynamics and unphysical results.

7.2 Symplectic maps

Considering a conservative accelerator system, meaning that there is no energy loss from synchrotron radiation or external time-dependent forces acting on it, Liouville's theorem states that the phase space area is conserved. This conservation is preserved only if the nonlinear maps used to represent the evolution of the particle's trajectories are symplectic. A transfer map is symplectic when the following condition is satisfied

$$J^T S J = S, \tag{I.9.47}$$

where J is the $n \times n$ Jacobian in the n-dimensional phase space

$$J = \begin{bmatrix} \frac{\partial x_f}{\partial x_i} & \frac{\partial x_f}{\partial p_{x_i}} & \cdots & \frac{\partial x_f}{\partial z_i} & \frac{\partial x_f}{\partial \delta_i} \\ \frac{\partial p_{x_f}}{\partial x_i} & \frac{\partial p_{x_f}}{\partial p_{x_i}} & \cdots & \frac{\partial p_{x_f}}{\partial z_i} & \frac{\partial p_{x_f}}{\partial \delta_i} \\ \vdots & \vdots & \ddots & \vdots & \vdots \\ \frac{\partial z_f}{\partial x_i} & \frac{\partial z_f}{\partial p_{x_i}} & \cdots & \frac{\partial z_f}{\partial z_i} & \frac{\partial z_f}{\partial \delta_i} \\ \frac{\partial \delta_f}{\partial x_i} & \frac{\partial \delta_f}{\partial p_{x_i}} & \cdots & \frac{\partial \delta_f}{\partial z_i} & \frac{\partial \delta_f}{\partial \delta_i} \end{bmatrix} \tag{I.9.48}$$

and S

$$S = \begin{bmatrix} I & 0 & \cdots & 0 \\ 0 & I & \cdots & 0 \\ \vdots & \vdots & \ddots & \vdots \\ 0 & 0 & \cdots & I \end{bmatrix},$$

with

$$I = \begin{bmatrix} 0 & 1 \\ -1 & 0 \end{bmatrix}.$$

An important property of the S matrix is that its determinant is 1 or -1: $\det(S) = 1$ if n is even or $\det(S) = -1$ if n is odd. From Eq. I.9.47 it follows that a transfer map is symplectic if the determinant of its Jacobian is equal to one

$$\det(J^T S J) = \det(S) \implies \det(J^T)\det(S)\det(J) = \det(S) \implies \det(J) = 1. \tag{I.9.49}$$

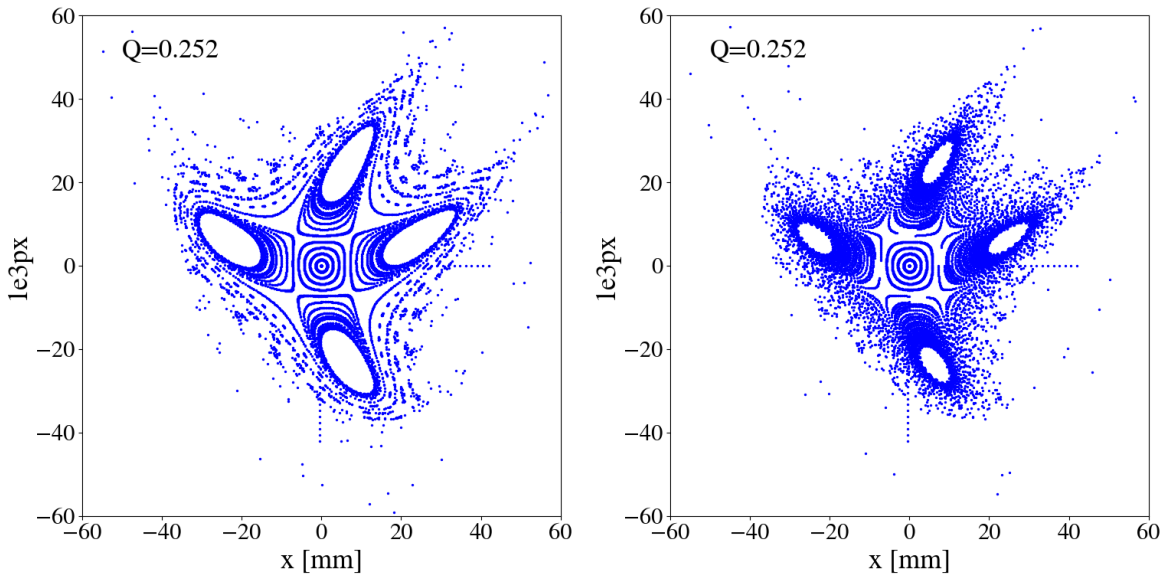

Fig. I.9.15: Phase space with symplectic (left) and non-symplectic (right) map.

When a power-series map is truncated to a finite order and loss of symplecticity occurs, the resulting phase space can be significantly different from the conditions in a real accelerator. Figure I.9.15 illustrates the phase space with a symplectic (left) and non-symplectic transfer map (right). In the first case the particle trajectories in the islands are well-defined by closed loops. However, in the second case, these loops become distorted, which could be interpreted as chaotic motion. This distortion may lead to inaccurate predictions of the particle stability and the overall beam lifetime in storage rings. The Python code of a symplectic and non-symplectic one-turn map for the simple example of a linear rotation and a sextupole kick can be found in the Appendix A.

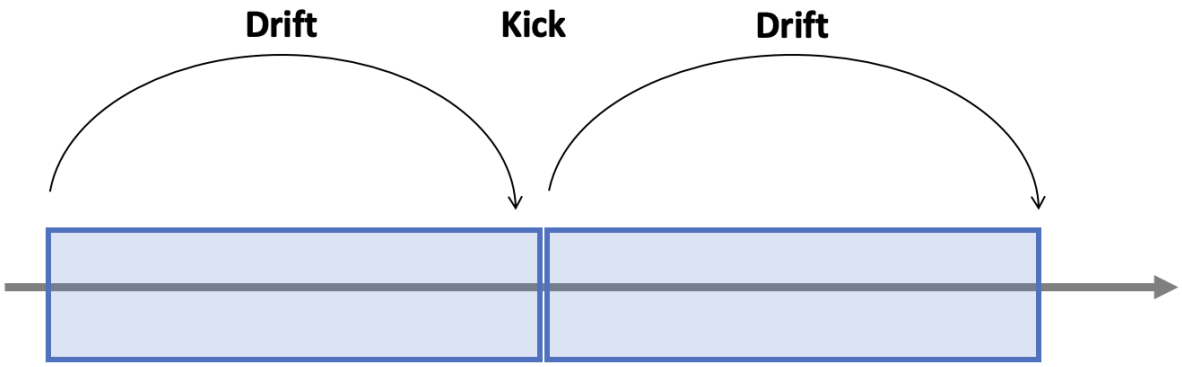

Fig. I.9.16: The concept of the "drift-kick-drift" symplectic integrator.

A powerful tool to preserve symplecticity in tracking codes is the use of symplectic integrators. For the case of a sextupole where

$$\frac{dx}{ds} = p_x, \quad \frac{dp_x}{ds} = -\frac{1}{2}k_2 x^2, \tag{I.9.50}$$

the nonlinear differential equations cannot be solved analytically to derive the equations of motion. An integrator that approximates the solution to these equations is used which splits the sextupole's influence into segments ("drift-kick-drift" approach). As shown in Fig. I.9.16, the integration is divided into three intervals: initial drift from 0 to $L/2$, a kick by a thin lens sextupole at $L/2$, and final drift from $L/2$ to L, where L is the sextupole length.

$$\begin{aligned}
&\text{For } 0 \le s < L/2: && x_1 = x_0 + \frac{L}{2}p_{x0}, \quad p_{x1} = p_{x0}, \\
&\text{For } s = L/2: && x_2 = x_1, \quad p_{x2} = p_{x1} - \frac{1}{2}k_2 L x_1^2, \\
&\text{For } L/2 \le s \le L: && x_3 = x_2 + \frac{L}{2}p_{x2}, \quad p_{x3} = p_{x2}.
\end{aligned} \tag{I.9.51}$$

Exercise 1

a) Derive the expression for the one-turn map in a lattice consisting of a linear rotation followed by a sextupole.

b) Show that this one-turn map is symplectic.

Hint: the Jacobian is:

$$J = \begin{bmatrix} \frac{\partial x'}{\partial x} & \frac{\partial x'}{\partial p_x} \\ \frac{\partial p'_x}{\partial x} & \frac{\partial p'_x}{\partial p_x} \end{bmatrix}.$$

c) Neglect the cross-term x and p_x on the one-turn map and demonstrate the loss of symplecticity.

Exercise 2

Take the transport matrix of a thick quadrupole and truncate the Taylor expansion up to first order. Is the map symplectic? How does it compare to the map of a thin quadrupole?

Hint: the transport map of a thick quadrupole is:

$$\mathcal{M}_Q = \begin{pmatrix} \cos(\sqrt{k}L) & \frac{1}{\sqrt{k}}\sin(\sqrt{k}L) \\ -\sqrt{k}\sin(\sqrt{k}L) & \cos(\sqrt{k}L) \end{pmatrix}. \tag{I.9.52}$$

8 Numerical methods

The evolution of particles through the elements of an accelerator over a large number of turns can be studied with tracking simulations. Tracking simulations allow to study the beam dynamics under a wide range of conditions and optimize the beam and machine configuration. By post-processing the tracking results, important information concerning the diffusion of the particle amplitude, the strength of the resonances and the particle's overall stability can be extracted. This section provides an overview of the main tools that are commonly used with tracking simulations. Of course, having a symplectic map of the accelerator under study is a pre-requisite.

8.1 Dynamic aperture

The dynamic aperture (DA) is closely correlated to the performance of a collider (or other circular accelerators) in operation. The DA represents the boundary between stable and unstable particle motion: particles with actions exceeding the DA are unstable and will eventually be lost, while particle inside the DA follow trajectories with long-term stability (those trajectories might however be chaotic). In simulations, the DA is obtained by tracking a large number of particles with different initial conditions and determining which particles are stable for a relevant number of turns (this depends on the accelerator and the required beam lifetime).

Figure I.9.17 illustrates the DA boundary for the Large Hadron Collider (LHC) based on simulations (blue and green) and measurements (red) at injection energy. Note the remarkable agreement between the simulation and the measurements. Here, the DA is calculated using symplectic tracking

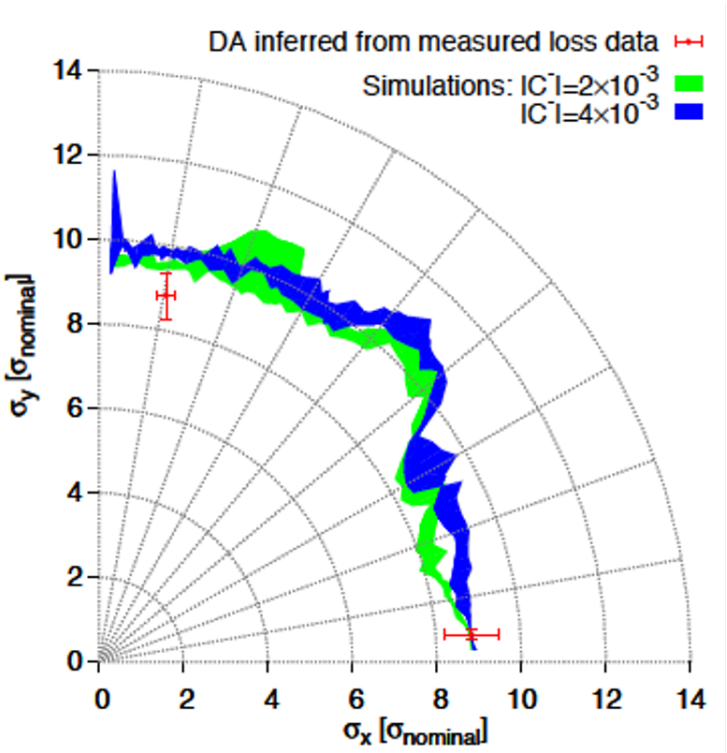

Fig. I.9.17: DA for the LHC from simulations (blue and green) and measurements (red) [17].

codes for 10^6 turns for the LHC. These simulations include multipole field errors and strong nonlinearities (such as beam-beam effects during collisions) that limit the area of stable motion. Since multipole errors are not always fully known, various machine models with random distributions of these errors are used to estimate them. Initial simulations may begin in 4D (transverse dimensions only) but typically need to extend to 5D (including constant energy deviation) and eventually 6D (including synchrotron motion).

The DA is an important guiding tool as it is strongly correlated to the beam lifetime in operation. Multi-parametric DA scans can be used to identify the optimal beam and machine parameters in operation in order to improve the beam lifetime. Figure I.9.18 depicts the horizontal tune as a function of the vertical tune for HL-LHC (the future upgrade of the LHC) and the color-code is the DA. Depending on the beam and machine parameters, some working points are more favorable (blue) while others leads to a reduction of the DA due to resonances (red) and should be avoided.

8.2 Numerical analysis of fundamental frequencies

The numerical analysis of fundamental frequencies (NAFF) was originally developed by J. Laskar to study chaotic motion within the solar system [18]. This algorithm can also be used to describe the quasi-periodic motion of particles in an accelerator described by symplectic maps. Compared to the traditional Fast Fourier Transform (FFT), the NAFF algorithm enhances the precision and accelerates the convergence when determining the amplitude, frequency, and phase of each component in a particle's

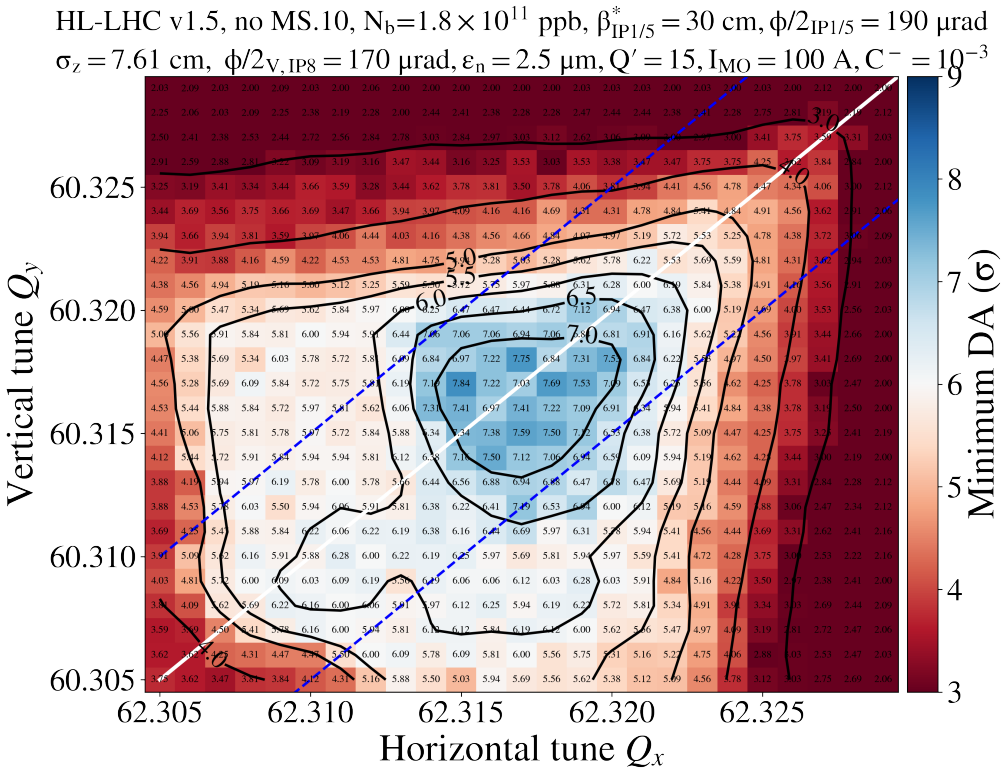

Fig. I.9.18: DA scan for the HL-LHC from simulations.

tune spectrum. This is achieved by maximizing the Fourier integral that is defined as

$$\phi(f) = \langle \psi(t), e^{i2\pi ft} \rangle = \frac{1}{T} \int_0^T \psi(t) e^{-i2\pi ft} x(t)\, dt, \tag{I.9.53}$$

where $\psi(t)$ is the quasi-periodic complex signal of the particle's position and momentum over a time interval $[0, T]$, f represents a specific frequency and $x(t)$ is the window function. The NAFF algorithm uses the Hann window to mitigate discontinuities at the edge of the signal's finite time span and suppress spectral leakage. The Hann window is defined as

$$x_h(t) = \frac{2^h (h!)^2 (1 + \cos \pi t)^h}{(2h)!}, \tag{I.9.54}$$

where h is the power of the window. Unlike the FFT, whose accuracy is proportional to $1/N$ (with N being the window's length), the precision of the NAFF algorithm improves with $1/N^{2h+2}$, particularly in the absence of noise in the signal and when the frequency components are well separated. The numerical integration is done using Hardy's 6-point integration rune and the refined frequency f_k, amplitude α_k and phase ϕ_k of the k-th spectral component are computed. The component is then subtracted from the signal and the search is iterated for additional spectral components. After iterating over N spectral

components, the quasi-periodic signal can be expressed as

$$\psi(t) = \sum_{k=1}^{N} a_k e^{i2\pi f_k t + \phi_k}. \tag{I.9.55}$$

A simplified version of the NAFF algorithm in Python can be found in the Appendix A.

8.3 Frequency map analysis

Frequency map analysis (FMA) is a powerful tool for detecting early signs of chaotic motion in the presence of nonlinearities [19–22]. This method involves tracking a distribution of particles, usually with initial conditions in the form of polar or rectangular grid in (x, y) and zero momenta, over a pre-defined number of turns. For instance, in the context of the LHC, 10000 turns are usually needed which corresponds to approximately 1 second in machine operation.

The turn-by-turn data of each particle are divided into two equal time intervals. The tune of each particle for both intervals is computed with the NAFF algorithm. The tune diffusion that reflects the tune variation between the two segments is then quantified using the "tune diffusion" defined as

$$D = \sqrt{(Q_x^1 - Q_x^2)^2 + (Q_y^1 - Q_y^2)^2}, \tag{I.9.56}$$

where Q_i^1, Q_i^2 with $i = (x, y)$ are the tunes from the first and second interval, respectively. The tunes of different particles are mapped onto a tune diagram, with a color code representing the logarithm of the tune diffusion.

Figure I.9.19 illustrates the FMA (left) and initial $x - y$ space (right) for the LHC color-coded with the tune diffusion. The resonances appear as lines in the tune domain and match the resonance condition indicated by the tune diagram (gray lines), while they appear as curves in the initial $x - y$ space. The origin of the large linear tune spread observed in the FMAs are the octupoles that are the main source of nonlinearity at injection energy and are crucial to maintain beam stability. Depending on the positive (top) or negative (bottom) polarity of the octupole current, particles with larger amplitudes will have a larger or lower tune, respectively, compared to the nominal tune working point. FMA allows to distinguish between the regions of stable (blue) and chaotic motion (red) as, due to the tune spread, some particles encounter strongly-driven resonances and start to diffuse in phase space and so their tune is not stable. This analysis allows to identify the strongest resonances and optimize for the best working point in operation.

9 Beam-beam effects

Apart from nonlinear magnets, one of the most significant sources of nonlinearities in particle colliders are beam-beam interactions [23]. The beams consist of charged particles that produce an electromagnetic field. When the two beams are in close proximity or intersecting, the electromagnetic field of one beam influences the other, resulting in a deflection of the particle trajectories. For round Gaussian beams, this

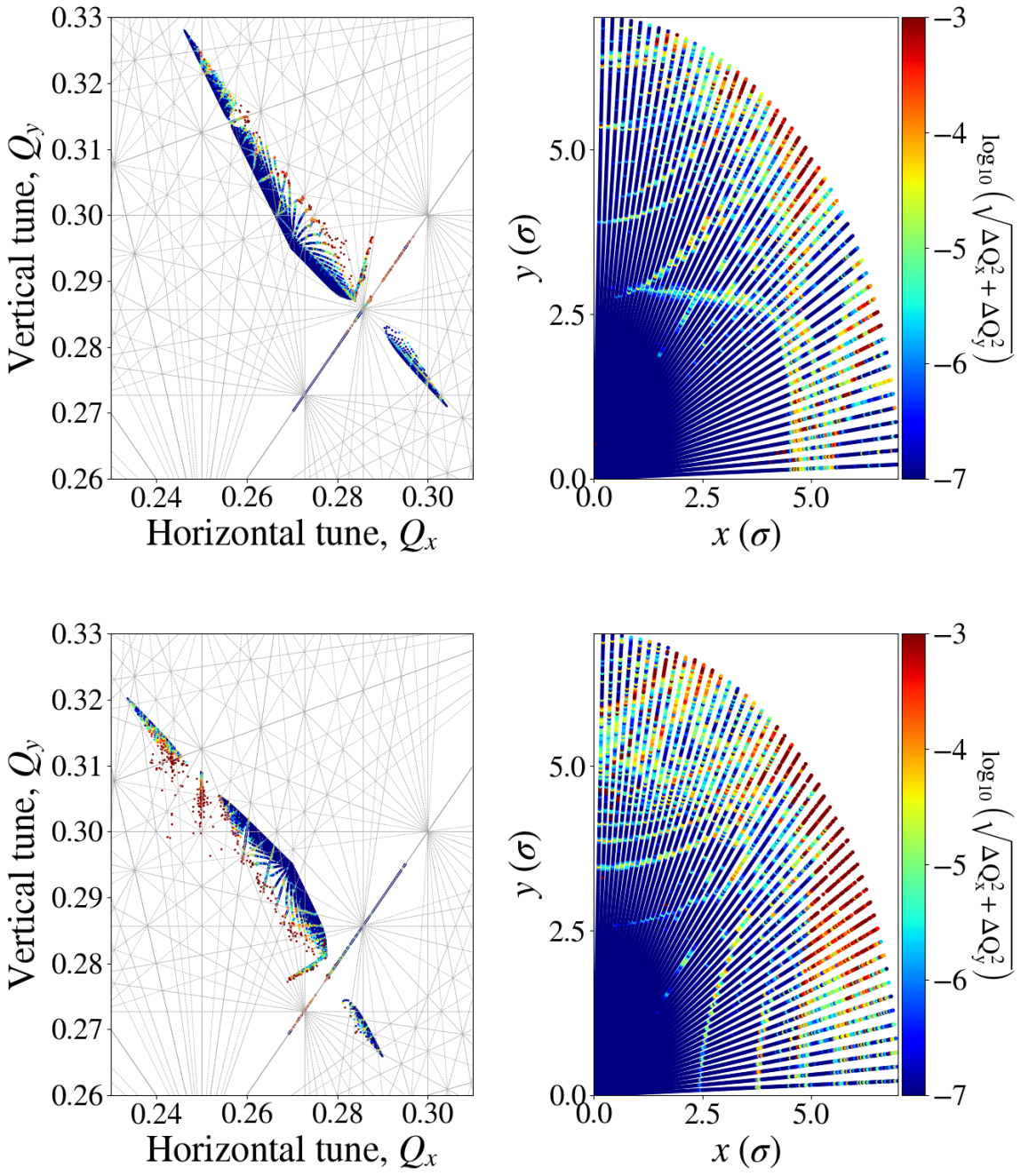

Fig. I.9.19: FMA for the LHC in the tune domain (left) and in the initial $x - y$ space (right) for positive (top) and negative (bottom) octupole polarities. The color-code represents the logarithm of the tune diffusion.

deflection can be expressed as

$$\Delta p_x = -\frac{2Nr_0}{\gamma} \cdot \frac{x}{r^2}\left[1 - \exp\left(-\frac{r^2}{2\sigma^2}\right)\right], \tag{I.9.57}$$

$$\Delta p_y = -\frac{2Nr_0}{\gamma} \cdot \frac{y}{r^2}\left[1 - \exp\left(-\frac{r^2}{2\sigma^2}\right)\right], \tag{I.9.58}$$

where r_0 is the classical particle radius, γ is the relativistic Lorentz factor, σ is the beam size, N is the number of particles in the bunch and $r = x^2 + y^2$.

For small particle amplitudes, i.e. when r is relatively small, the beam-beam force is approximately linear and thus similar to the force of a quadrupole, a regime known as the *head-on* beam-beam interaction. The intensity of this linear interaction is represented by the linear beam-beam parameter, which indicates the tune shift, and for round Gaussian beams is given by

$$\xi = \frac{Nr_0\beta^*}{4\pi\gamma\sigma^2}, \tag{I.9.59}$$

where β^* is the β-function at the collision point. As the amplitude increases, the force becomes nonlinear, a regime known as *long-range* interaction, leading to a tune spread that varies with amplitude and can be approximated by

$$\Delta Q_{lr} \propto \frac{N}{d^2}, \tag{I.9.60}$$

where d is the distance of the two bunches. Beam-beam effects challenge the collider's performance due to their tendency to:

– Induce a large tune spread, causing particles to cross multiple resonances in the tune diagram;

– Excite resonances up to very high orders.

The FMA of the LHC in the presence of beam-beam is shown in Fig. I.9.20. Due to the large tune spread, particles are crossing the diagonal and, due to the important strength of the resonance, a large number of particles is lost.

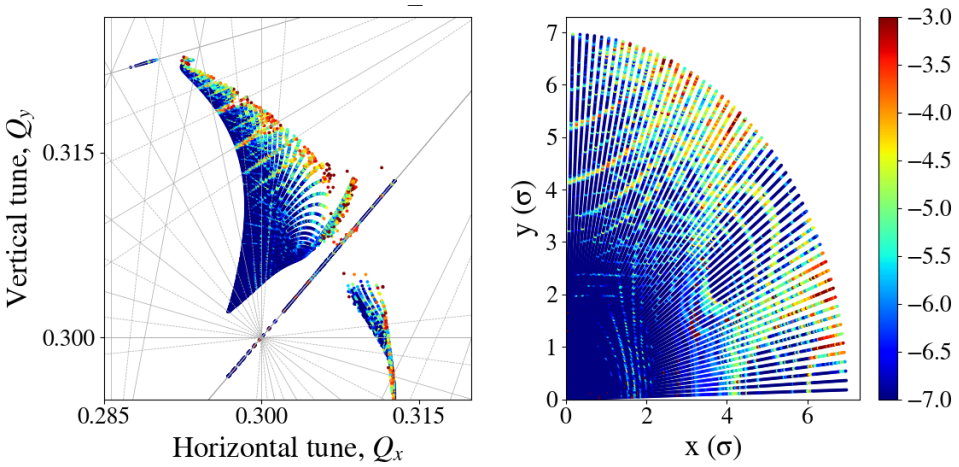

Fig. I.9.20: FMA for the LHC in the tune domain (left) and in the initial $x - y$ space (right) in the presence of beam-beam interactions. The color-code represents the logarithm of the tune diffusion.

To mitigate parasitic beam-beam interactions away from the collision points, the beams are colliding with a crossing angle, as depicted in Fig. I.9.21. Besides head-on collisions at the interaction points,

bunches in close proximity within the shared vacuum pipe experience long-range interactions. These can be mitigated by increasing the crossing angle at the cost of the collider's performance, as the overlap between the two beams reduces, reducing the number of collisions. In the same context, increasing the collision rate requires small and intense beams which, in turn, leads to a significant tune spread due to head-on beam-beam effects. Therefore, beam-beam studies, often based on DA analysis, are essential for balancing the mitigation of beam-beam effects with the optimization of the collider performance.

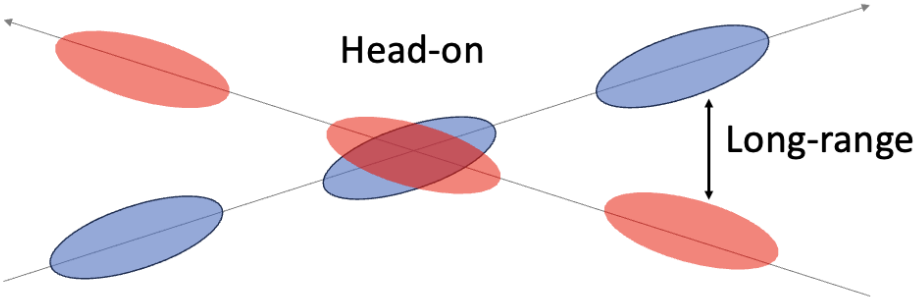

Fig. I.9.21: The head-on and long-range beam-beam interaction in the presence of a crossing angle.

10 Tune modulation

When particles are not influenced by resonances, they exhibit stable and predictable paths, characterized by constant betatron tunes. This ideal state can be perturbed by various phenomena such as tune modulation. Tune modulation refers to the periodic variation of the betatron tune in time

$$Q_{\text{inst}}(n) = Q_0 + \Delta Q \cos(2\pi Q_m n), \tag{I.9.61}$$

where Q_0 is the tune in the absence of a tune modulation, ΔQ is the maximum deviation of the betatron tune from its unperturbed value, Q_m is the modulation frequency (in units of 2π as the betatron tune) and n the turn number. This modulation can be the result of several effects such as:

- Synchro-betatron coupling from chromaticity: passing through quadrupoles, particles with different longitudinal momentum deviations will experience different focusing due to chromaticity. At the same time, they undergo synchrotron oscillations at the synchrotron frequency in the longitudinal plane, which leads to a periodic variation of their momentum deviations. During each revolution, the particles go through the quadrupoles with a different momentum deviation, which leads to the modulation of the betatron frequency with the synchrotron tune. This interaction between the longitudinal and transverse plane is known as synchro-betatron coupling. The maximum variation of the tune from its unperturbed value is proportional to the chromaticity and the peak momentum deviation.

- Beam-beam interactions and synchro-betatron coupling: the effect of beam-beam interactions depend on the position of the particle within the bunch. Due to synchrotron oscillations, a particle initially at the head of the bunch that might experience a strong beam-beam kick will eventually

be at the tail and experience a different beam-beam interaction. The variation of the beam-beam force as particles oscillate longitudinally induces synchro-betatron coupling.

– Power supply ripple: power supply ripples are fluctuations in the voltage output of magnet power supplies with a specific frequency that is usually a harmonic of the mains frequency 50 Hz. These fluctuations translate into variations in the magnet current, which cause perturbations in the magnetic field. In the case of quadrupoles, this leads to a modulation of the magnet focusing strengths. When the focusing strength of a quadrupole is not constant, the particles will encounter a different focusing at each revolution, which, in turn, modulates the particles' betatron tune. This type of modulation appears in the beam spectrum as sidebands of 50 Hz harmonics around the betatron tune. The maximum tune variation from the unperturbed tune is proportional to the beta-function at the location of the modulated quadrupole.

Tune modulation has significant implications for the performance of a collider, as its interplay with nonlinearities results in the excitation of additional resonances, reducing even further the resonance-free regions in the tune diagram. This can be illustrated with a simplified lattice that includes a linear rotation and an octupole that excites the sixth-order resonance and the tune is close to the resonance. Figure I.9.22 (top left) shows the action-angle variables (first panel) and the variation of the tune with action (second panel). The tune is changing linearly with the action as a result of the amplitude detuning induced by the octupoles and some particles are trapped in the $6Q_x = 2$ resonance. Introducing a modulated quadrupole with a modulation frequency equal to Q_m (middle) results in the appearance of additional resonance islands. For slower modulation frequency, many islands of high-order resonance sidebands ($n \cdot Q_m$ with $n = 1, 2 \ldots 5$) appear (bottom). In this case, the islands of the main resonance and the resonance sidebands are overlapping and, as described in the previous sections, resonance overlap occurs resulting in chaotic motion.

In the general two-dimensional case in the presence of tune modulation, the resonance condition of Eq. I.9.29 takes the form

$$n_x Q_x + n_y Q_y + n_m Q_m = r. \tag{I.9.62}$$

The resonances described by the additional term appear as sideband resonances at a distance equal to multiples n_m of the modulation frequency. Their strength depends on the strength of the main resonances with which they are associated. Depending on the modulation frequency and their strength, the sideband resonances can either be very close to each other or to the main resonances and overlap, leading to chaotic motion, or reach the tune footprint even if the modulation frequency is far away from the betatron tune, acting as an additional diffusion mechanism for the particles in the distribution. This is illustrated with the FMAs for a specific configuration of the LHC at CERN in Fig. I.9.23 where the color-code indicates the tune diffusion. A comparison between the unperturbed case in the absence of a tune modulation and the case where a tune modulation is present due to power supply ripple in a quadrupole with a frequency of 100 Hz (neglecting the impact of synchrotron motion) reveals that a strong resonance $Q_x - Q_y + Q_m = 0$ is excited, mainly impacting the particles at larger amplitudes. If the modulation frequency is changed to 600 Hz, then another strong resonance reaches the footprint ($Q_x - 2Q_y + Q_m = 1$) and mainly affects particles with lower amplitudes. This example shows that certain modulation frequencies may be more critical than others depending on the working point.

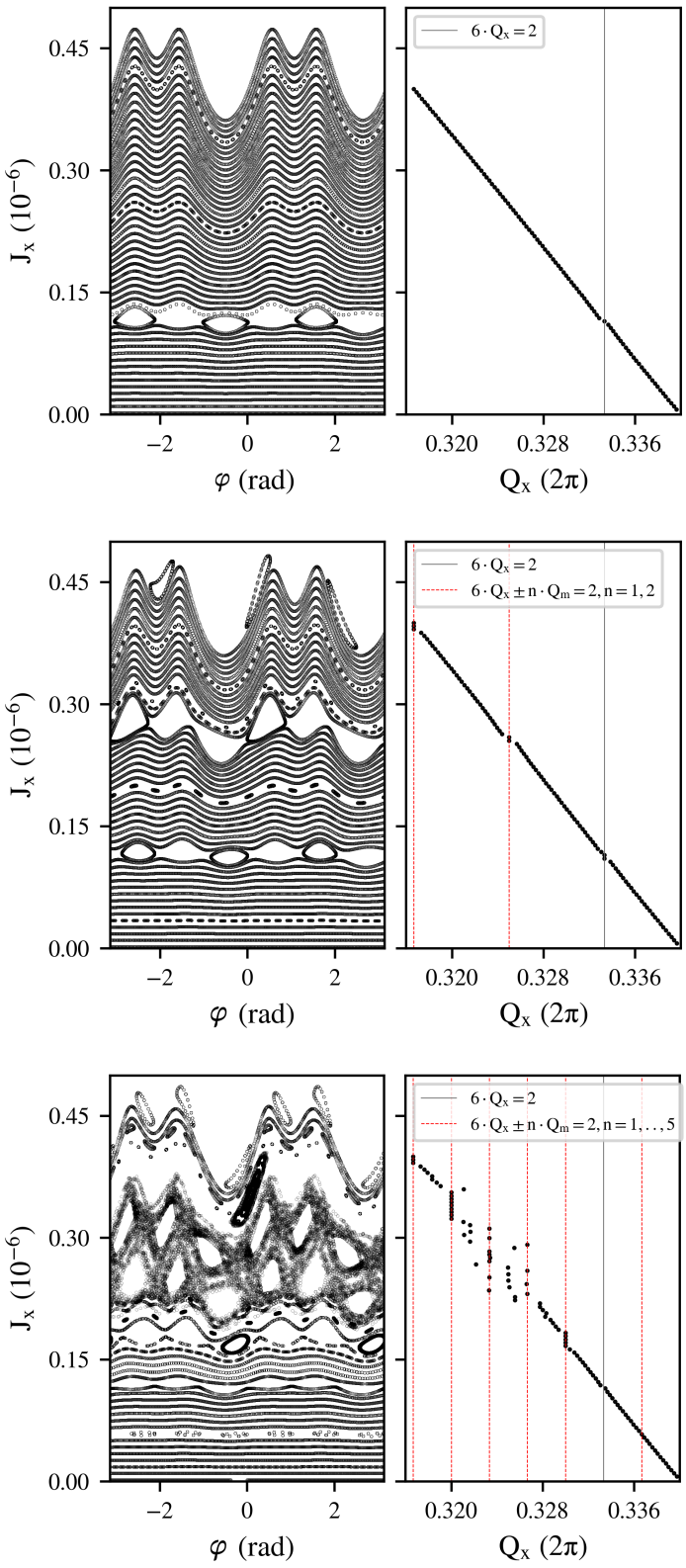

Fig. I.9.22: Action-angle variables (first panel) and tune variation with action (second panel) for a simple lattice including a linear rotation and an octupole (top), adding a modulated quadrupole with a modulation frequency Q_m (middle) and a reduced Q_m (bottom) [24]. The tune of the particles trapped on the main islands (vertical black line) and sideband islands (vertical red line) is also illustrated.

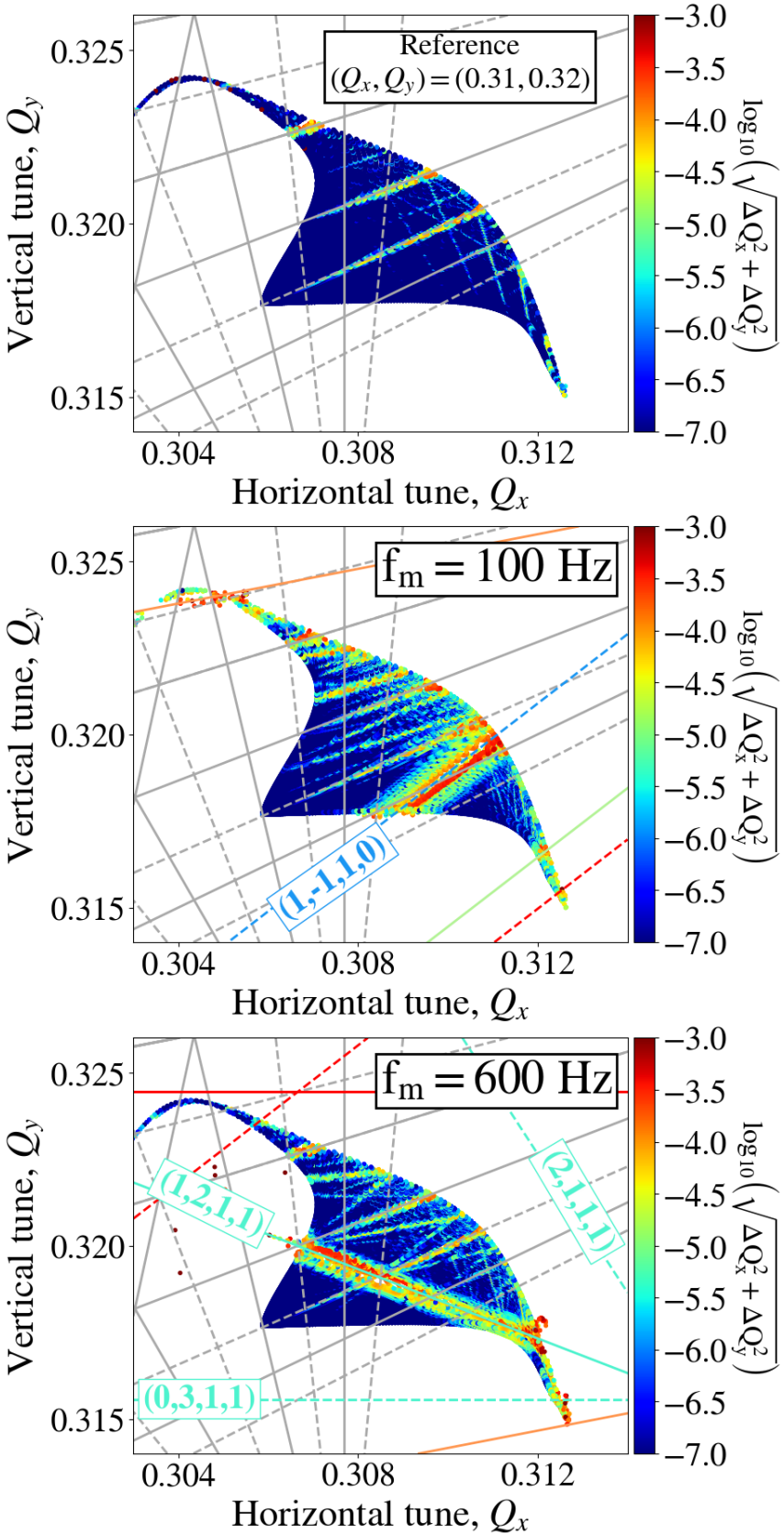

Fig. I.9.23: FMAS for the LHC at CERN without tune modulation (top), with tune modulation due to quadrupole power supply ripple at 100 Hz (middle) and 600 Hz (bottom) [24]. The main resonances are depicted in gray and the sideband resonances in red, blue and cyan.

11 Beam extraction with resonances

Despite their negative implications, resonances can also be used to extract particles from a synchrotron for various experimental needs. Some of these methods are the slow extraction, multi-turn extraction and the resonant fast extraction. As an example, several fixed-target facilities receive beams from the LHC injector complex, complementary to the LHC, and the beam is extracted by exploiting resonances.

Resonant slow extraction is a method to extract the beam in a continuous way over an extended period of time, typically several seconds. A typical use of slow extraction is the beam extraction in the CERN Super Proton Synchrotron (SPS), where the beam is extracted over 4.8 s towards the fixed-target experiments of the North Area. The working principle is depicted in the evolution of the phase space in Fig. I.9.24. As a first step, a closed-orbit bump is used to displace the beam closer to the extraction septum, which is an element that separates the circulating from the extracted beam (top left and middle). Then, sextupole magnets are powered to excite the third-order resonance (top right). At the same time, the momentum spread in the distribution is increased with radio-frequency manipulations, which, in the presence of chromaticity, is translated into a large tune spread. The machine tune is initially set to a value below the resonance and, by changing the current of the main quadrupoles, the tune is dynamically changed (bottom). Depending on the momentum, the chromaticity and the machine tune, some particles move closer to the separatrix, become unstable and are guided out of the accelerator through the septum. The tune of the machine is then slowly changed to extract the remaining particles. This technique creates a continuous "spill" of particles that is then deflected into the transfer line headed to the fixed-target experiments.

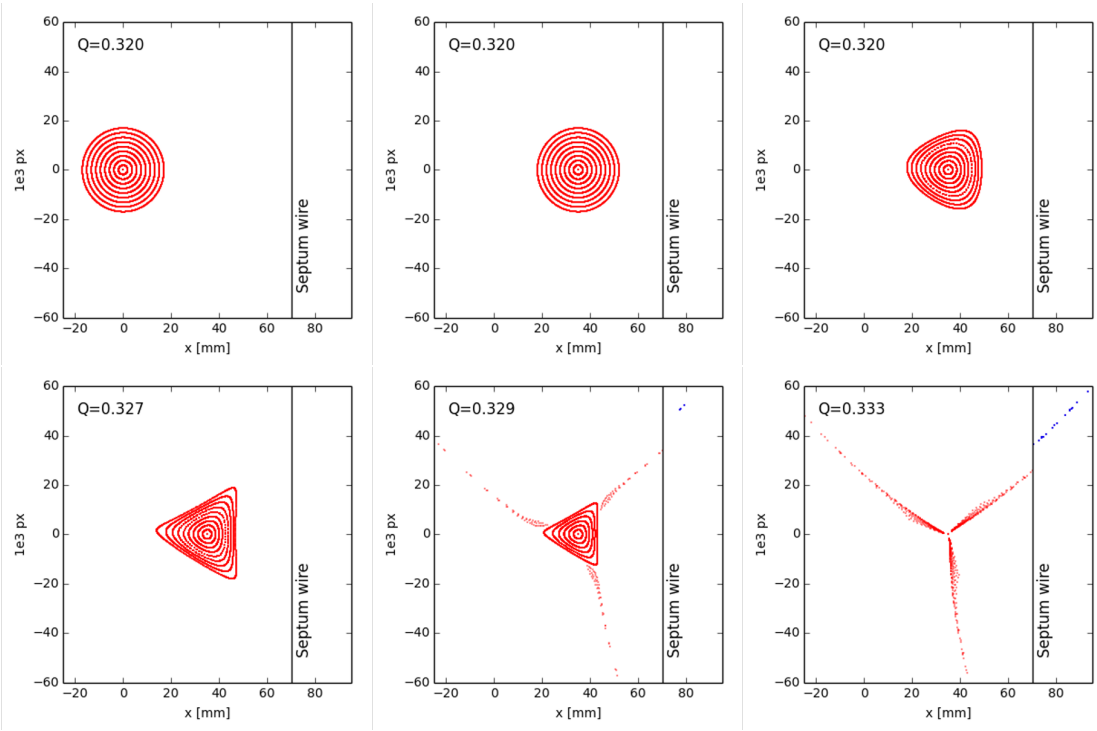

Fig. I.9.24: The basic working principle of the slow resonant extraction.

Another method is the Resonant Multi-Turn Extraction (MTE) [26]. MTE was originally developed to improve the efficiency of the beam extraction from the Proton Synchrotron (PS) to the SPS at CERN, and it has been systematically used in operation since 2015. The previous extraction method used since 1973, referred to as Continuous Transfer, included physical slicing of the beam on the septum, resulting in high levels of machine activation due to radiation. In the MTE technique, sextupole and octupole magnets are used to excite a fourth order resonance and create islands in the horizontal phase space as illustrated in Fig. I.9.25. By ramping the horizontal tune, some particles are trapped in the islands while other remain at the core (top right). The particles trapped inside the islands are then moved towards larger amplitudes (middle). The current in the sextupole and octupole is then decreased while the tune increases and the islands are even further separated from the core (bottom). Once the islands are sufficiently separated, the beam is extracted over a duration of four turns for the islands and one turn for the core.

Finally, another method of resonance extraction is the resonance fast extraction method used in the SPS at CERN. In the resonant fast extraction, the current in the quadrupoles is adjusted so that the machine tune is close to the half-integer. Octupoles are used to excite the half-integer resonance. Then, a fast discharge in the quadrupole current pushes the particles' tune onto the resonance. The particles are extracted in streams, over a few ms.

12 Conclusions

The beam dynamics in accelerators is significantly influenced by nonlinear effects. Nonlinearities, originating from various sources such as nonlinear magnets used to control various beam properties or as an unavoidable consequence of the beam-beam interactions, introduce amplitude detuning and, more importantly, they excite resonances. In the vicinity of a resonance, a review of the phase space reveals the existence of fixed and unstable points. When unstable points are perturbed, they can lead to chaotic motion. Rapid diffusion is also observed when resonance overlap occurs. In some cases, it is possible to compensate for individual resonances either with the lattice design or with dedicated corrector magnets. Understanding the impact of nonlinear effects often requires symplectic tracking simulations. Tools such as Dynamic Aperture and Frequency Map Analysis are powerful techniques to optimize the beam and machine parameters and eventually reduce the negative effects of resonances. Despite their challenges, resonances are also used for controlled beam extractions.

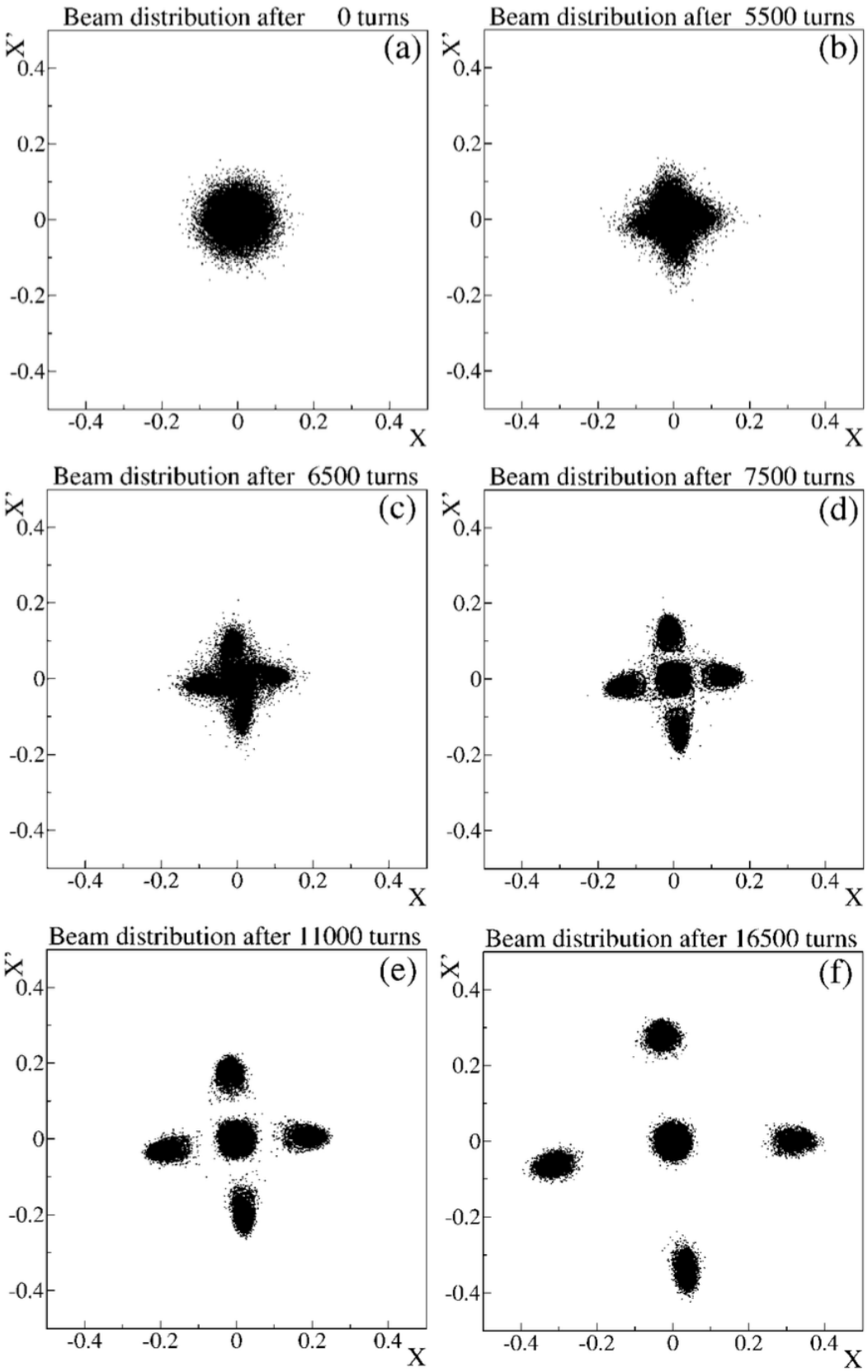

Fig. I.9.25: The working principle of the MTE [27].

A Python code for simplified model

Listing I.9.1: Simple accelerator class.

```
import numpy as np
import matplotlib.pyplot as plt
import pandas as pd

class simple_accelerator:
    def __init__(self, mu_x, initial_particle_coordinates, k2l=0, k3l
       =0):
        self.mu_x = mu_x
        self.k2l = k2l
        self.k3l = k3l
        self.particle_coordinates = np.atleast_2d(
           initial_particle_coordinates)
        self.turns = 0

    def apply_rotation(self):
        cos_mu = np.cos(self.mu_x)
        sin_mu = np.sin(self.mu_x)
        x_new = self.particle_coordinates[:, 0] * cos_mu + self.
           particle_coordinates[:, 1] * sin_mu
        px_new = -self.particle_coordinates[:, 0] * sin_mu + self.
           particle_coordinates[:, 1] * cos_mu
        self.particle_coordinates = np.column_stack((x_new, px_new))

    def apply_sextupole_kick(self):
        self.particle_coordinates[:, 1] -= 0.5 * self.k2l * self.
           particle_coordinates[:, 0]**2

    def apply_octupole_kick(self):
        self.particle_coordinates[:, 1] -= (1/6) * self.k3l * self.
           particle_coordinates[:, 0]**3

    def initialize_turn_by_turn_data(self, number_of_turns=100):
        self.turn_by_turn_data = np.zeros((number_of_turns+1, self.
           particle_coordinates.shape[0], 2))
        self.turn_by_turn_data[0] = self.particle_coordinates

    def save_particle_coordinates(self):
        self.turn_by_turn_data[self.turns] = self.
           particle_coordinates
```

```
    def get_turn_by_turn_pandas(self):
        flat_data = self.turn_by_turn_data.reshape(-1, 2)
        number_of_particles = self.particle_coordinates.shape[0]
        turn_nb = np.repeat(np.arange(self.turns + 1),
            number_of_particles)
        particle_id = np.tile(np.arange(number_of_particles), self.
            turns+1)
        return pd.DataFrame({
            'x': flat_data[:, 0],
            'px': flat_data[:, 1],
            'action': 0.5 * (flat_data[:, 0]**2 + flat_data[:, 1]**2)
                ,
            'angle': np.arctan2(flat_data[:, 1], flat_data[:, 0]),
            'turn nb': turn_nb,
            'particle id': particle_id
        }, index=[particle_id]).sort_index()

    def compute_particle_tune(self, group):
        fourier = np.fft.rfft(group['x'].values - np.mean(group['x'].
            values))
        frequencies = np.fft.rfftfreq(n=len(group), d=1.0)
        max_frequency = frequencies[np.argmax(np.abs(fourier))]
        return max_frequency
```

Listing I.9.2: Phase space.

```
number_of_particles = 20
x_min = 6e-7
x_max = 0.042
x = np.linspace(x_min, x_max, number_of_particles)
px = np.zeros(number_of_particles)
initial_particle_coordinates = np.column_stack((x, px))

k2l = -45.0
k3l = 0.
mu_x = (2.0*np.pi*0.403)
number_of_turns = 10000

accelerator = simple_accelerator(mu_x, initial_particle_coordinates,
    k2l=k2l, k3l=k3l)
```

```
accelerator.initialize_turn_by_turn_data(number_of_turns)
modulated_strength = []
for turn in range(number_of_turns):
    accelerator.apply_rotation()
    accelerator.apply_sextupole_kick()
    accelerator.apply_octupole_kick()
    accelerator.turns += 1
    accelerator.save_particle_coordinates()

turn_by_turn_data = accelerator.get_turn_by_turn_pandas()
particle_tunes = turn_by_turn_data.groupby('particle id').apply(
   accelerator.compute_particle_tune)

fig, ax = plt.subplots(figsize=(8,8))
plt.scatter(turn_by_turn_data.x*1e3, turn_by_turn_data.px*1e3, c="b",
    s=2)
plt.ylim(-60, 60)
plt.xlim(-60, 60)
plt.xlabel("x [mm]")
plt.ylabel("1e3px")
plt.text(-50,50, f"Q={mu_x/(2.0*np.pi):.3f}", fontsize=25)
```

Listing I.9.3: Action-angle and tune.

```
number_of_particles = 30
min_action = 1e-10
max_action = 13e-5

actions = np.linspace(min_action, max_action, number_of_particles)
phi = np.deg2rad(45.0)

initial_particle_coordinates = np.zeros((number_of_particles, 2))

for i, J in enumerate(actions):
    x = np.sqrt(2 * J) * np.cos(phi)
    px = np.sqrt(2 * J) * np.sin(phi)
    initial_particle_coordinates[i] = [x, px]

k21 = 0
k31 = 80*100.
mu_x = (2.0*np.pi*0.244)
number_of_turns = 10000
```

```
accelerator = simple_accelerator(mu_x, initial_particle_coordinates,
    k2l=k2l, k3l=k3l)

accelerator.initialize_turn_by_turn_data(number_of_turns)
for turn in range(number_of_turns):
    accelerator.apply_rotation()
    accelerator.apply_sextupole_kick()
    accelerator.apply_octupole_kick()
    accelerator.turns += 1
    accelerator.save_particle_coordinates()

turn_by_turn_data = accelerator.get_turn_by_turn_pandas()
particle_tunes = turn_by_turn_data.groupby('particle id').apply(
    accelerator.compute_particle_tune)

fig, ax = plt.subplots(ncols=2, figsize=(10, 6))
plt.sca(ax[0])
plt.scatter(turn_by_turn_data.x*1e3, turn_by_turn_data.px*1e3, c="b",
    s=1)
plt.ylim(-20, 20)
plt.xlim(-20, 20)
plt.xlabel("x [mm]")
plt.ylabel("1e3px")
plt.text(-10,17, f"Q={mu_x/(2.0*np.pi):.3f}", fontsize=25)

plt.sca(ax[1])
data_at_turn_0 = turn_by_turn_data[turn_by_turn_data['turn nb'] == 0]
plt.plot(data_at_turn_0.action*1e6*2., particle_tunes, c="b", ms=5,
    marker="o")
plt.axhline(0.25,c="r", lw=0.5)
plt.ylabel(r"$Q_x$")
plt.xlabel(r"2J$_x$ [um]")
```

Listing I.9.4: Simplified NAFF algorithm.

```
import numpy as np
from scipy.optimize import minimize_scalar

def hann_window(t, h=1):
    return (2**h * np.math.factorial(h)**2 * (1 + np.cos(np.pi * t /
        t[-1]))**h) / np.math.factorial(2*h)
```

```
def discrete_fourier_integral(signal, times, freq, h=1):
    exp_factor = np.exp(-1j * 2 * np.pi * freq * times)
    my_hann_window = hann_window(times, h=h)
    integral = np.sum(my_hann_window * signal * exp_factor)
    return integral

def simple_naff(signal, times, h=1):
    def objective(freq):
        return -np.abs(discrete_fourier_integral(signal, times, freq,
            h=h))

    freq_bounds = (0, 0.5 * (1 / np.mean(np.diff(times))))
    result = minimize_scalar(objective, bounds=freq_bounds, method='
       bounded')
    dominant_freq = result.x

    complex_fourier_integral = discrete_fourier_integral(signal,
       times, dominant_freq, h=h)
    dominant_amplitude = abs(complex_fourier_integral)/len(times)*2
    return dominant_freq, dominant_amplitude

# Example
revolution_frequency = 11245.5
number_of_turns = 10000
duration = number_of_turns * 1/revolution_frequency
times = np.linspace(0, duration, number_of_turns, endpoint=False)
frequency = 3000
signal = 20.0*np.sin(2 * np.pi * frequency * times)

dominant_freq= simple_naff(signal, times, h=3)
print(f"Main frequency: {dominant_freq[0]} Hz")
```

Listing I.9.5: One-turn map and non-symplectic maps.

```
import sympy as sp

class simple_accelerator_oneturn:
    def __init__(self, mu_x, initial_particle_coordinates, k21=0, k31
       =0):
        self.mu_x = mu_x
```

```
        self.k2l = k2l
        self.k3l = k3l
        self.particle_coordinates = np.atleast_2d(
            initial_particle_coordinates)
        self.turns = 0

    def initialize_turn_by_turn_data(self, number_of_turns=100):
        self.turn_by_turn_data = np.zeros((number_of_turns+1, self.
            particle_coordinates.shape[0], 2))
        self.turn_by_turn_data[0] = self.particle_coordinates

    def save_particle_coordinates(self):
        self.turn_by_turn_data[self.turns] = self.
            particle_coordinates

    def get_turn_by_turn_pandas(self):
        flat_data = self.turn_by_turn_data.reshape(-1, 2)
        number_of_particles = self.particle_coordinates.shape[0]
        turn_nb = np.repeat(np.arange(self.turns + 1),
            number_of_particles)
        particle_id = np.tile(np.arange(number_of_particles), self.
            turns+1)
        return pd.DataFrame({
            'x': flat_data[:, 0],
            'px': flat_data[:, 1],
            'action': 0.5 * (flat_data[:, 0]**2 + flat_data[:, 1]**2)
                ,
            'angle': np.arctan2(flat_data[:, 1], flat_data[:, 0]),
            'turn nb': turn_nb,
            'particle id': particle_id
        }, index=[particle_id]).sort_index()

    def check_symplecticity(self, x_rot, px_kick):
        x, px, mu_x, k2l = sp.symbols('x p_x mu_x k2l')
        map = sp.Matrix([x_rot, px_kick])
        variables = sp.Matrix([x, px])
        jacobian = map.jacobian(variables)#.simplify()
        print("Jacobian:")
        sp.pprint(jacobian)
        det_jacobian = jacobian.det().simplify()
        print()
```

```
        print("Determinant of Jacobian:")
        sp.pprint(det_jacobian)
        is_symplectic = sp.simplify(det_jacobian) == 1
        print()
        print(f"The map is symplectic: {is_symplectic}")

    def define_one_turn_symplectic(self):
        x, px, k2l, mu_x = sp.symbols('x p_x k_{2l} mu_x')
        cos_mu = sp.cos(mu_x)
        sin_mu = sp.sin(mu_x)
        x_rot  = x * cos_mu + px * sin_mu
        px_rot  = -x * sin_mu + px * cos_mu
        px_sext = px_rot - 0.5*k2l * x_rot**2
        self.check_symplecticity(x_rot, px_sext)
        return x_rot, px_sext, x , px, k2l, mu_x

    def truncate_expression(self, expr, x, px, x_order=2, px_order=2)
        :
        truncated_expr = 0
        for term in expr.as_ordered_terms():
            powers = term.as_powers_dict()
            if powers.get(x, 0) <= x_order and powers.get(px, 0) <=
                px_order:
                if powers.get(x, 0) != powers.get(px, 0):
                    truncated_expr += term
        return truncated_expr

    def define_one_turn_truncated(self):
        x, px, k2l, mu_x = sp.symbols('x p_x k_{2l} mu_x')
        cos_mu = sp.cos(mu_x)
        sin_mu = sp.sin(mu_x)
        x_rot  = x * cos_mu + px * sin_mu
        px_rot  = -x * sin_mu + px * cos_mu
        px_sext = px_rot - 0.5*k2l * x_rot**2
        px_sext = self.truncate_expression(px_sext.expand(), x, px)
        self.check_symplecticity(x_rot, px_sext)
        return x_rot, px_sext, x , px, k2l, mu_x


number_of_particles = 30
x_min = 6e-7
```

```
x_max = 0.042
x = np.linspace(x_min, x_max, number_of_particles)
px = np.zeros(number_of_particles)
initial_particle_coordinates = np.column_stack((x, px))

k2l = -0.45*100
mu_x = (2.0*np.pi*0.252)

number_of_turns = 500

accelerator_oneturn = simple_accelerator_oneturn(mu_x,
    initial_particle_coordinates, k2l=k2l)
accelerator_oneturn.initialize_turn_by_turn_data(number_of_turns)

#x_rot, px_kick, sp_x, sp_px, sp_k2l, sp_mux = accelerator_oneturn.
    define_one_turn_symplectic()
x_rot, px_kick, sp_x, sp_px, sp_k2l, sp_mux = accelerator_oneturn.
    define_one_turn_truncated()

print()
print("One turn maps for x and px:")
print("x\' = ")
sp.pprint(x_rot.expand().simplify())
print("px\' = ")
sp.pprint(px_kick.expand().simplify())


for turn in range(number_of_turns):
    print(turn, number_of_turns)
    new_x = [x_rot.subs({sp_x: x_val, sp_px: px_val, sp_k2l: k2l,
        sp_mux:mu_x }).evalf() for x_val, px_val in
        accelerator_oneturn.particle_coordinates]
    new_px = [px_kick.subs({sp_x: x_val, sp_px: px_val, sp_k2l: k2l,
        sp_mux:mu_x}).evalf() for x_val, px_val in accelerator_oneturn
        .particle_coordinates]

    accelerator_oneturn.particle_coordinates = np.array([new_x,
        new_px]).T
    accelerator_oneturn.turns += 1
    accelerator_oneturn.save_particle_coordinates()
```

```
turn_by_turn_data_oneturn = accelerator_oneturn.
    get_turn_by_turn_pandas()

fig, ax = plt.subplots(figsize=(8,8))
plt.scatter(turn_by_turn_data_oneturn.x*1e3,
    turn_by_turn_data_oneturn.px*1e3, c="b", s=2)
plt.ylim(-60, 60)
plt.xlim(-60, 60)
plt.xlabel("x [mm]")
plt.ylabel("1e3px")
plt.text(-50,50, f"Q={mu_x/(2.0*np.pi):.3f}", fontsize=25)
```

B Solution to the exercises

B.1 Exercice 1

The Python code for the symplectic and non-symplectic one-turn maps can be found in the Appendix A.

a) **One-turn map:** In a lattice consisting of a linear rotation and a sextupole, the one-turn map can be derived as follows. First, the linear rotation is applied

$$x' = x\cos(\mu_x) + p_x\sin(\mu_x),$$
$$p'_x = -x\sin(\mu_x) + p_x\cos(\mu_x),$$

where $\mu_x = 2\pi Q_x$ represents the total phase advance with Q_x being the betatron tune. Then, a sextupole kick is applied, affecting only the momentum

$$p''_x = p'_x - \frac{1}{2}k_{2l}x'^2.$$

The one-turn map is

$$\begin{aligned} x' &= p_x\cdot\sin(\mu_x) + x\cdot\cos(\mu_x),\\ p''_x &= -0.5\cdot k_{2l}\cdot p_x^2\cdot\sin^2(\mu_x) - 0.5\cdot k_{2l}\cdot x^2\cdot\cos^2(\mu_x) + p_x\cdot\cos(\mu_x) - x\cdot\sin(\mu_x)\\ &\quad - 0.5\cdot k_{2l}\cdot p_x\cdot x\cdot\sin(2\mu_x). \end{aligned}$$

b) **Demonstrating symplecticity:** the one-turn map is symplectic if the determinant of its Jacobian is equal to one. The Jacobian J is defined as

$$J = \begin{bmatrix} \frac{\partial x'}{\partial x} & \frac{\partial x'}{\partial p_x} \\ \frac{\partial p'_x}{\partial x} & \frac{\partial p'_x}{\partial p_x} \end{bmatrix}.$$

The Jacobian for this one-turn map is

$$J = \begin{bmatrix} \cos(\mu_x) & \sin(\mu_x) \\ -k_{2l}\cdot(p_x\sin(\mu_x) + x\cos(\mu_x))\cdot\cos(\mu_x) - \sin(\mu_x) & -k_{2l}\cdot(p_x\sin(\mu_x) + x\cos(\mu_x))\cdot\sin(\mu_x) + \cos(\mu_x) \end{bmatrix}.$$

The determinant of the Jacobian matrix J is calculated as follows

$$\begin{aligned}\det(J) &= \cos(\mu_x)\cdot[-k_{2l}\cdot(p_x\sin(\mu_x)+x\cos(\mu_x))\cdot\sin(\mu_x)+\cos(\mu_x)]\\ &\quad-\sin(\mu_x)\cdot[-k_{2l}\cdot(p_x\cdot\sin(\mu_x)+x\cdot\cos(\mu_x))\cdot\cos(\mu_x)-\sin(\mu_x)]\\ &= \cos^2(\mu_x)+\sin^2(\mu_x)\\ &= 1.\end{aligned}$$

Therefore, the transformation is symplectic as

$$\det(J) = 1.$$

c) **Neglecting terms:** after neglecting the term involving the product of x and p_x, the expression for p_x'' is simplified to

$$p_x'' = -0.5\cdot k_{2l}\cdot p_x^2\cdot\sin^2(\mu_x) - 0.5\cdot k_{2l}\cdot x^2\cdot\cos^2(\mu_x) + p_x\cdot\cos(\mu_x) - x\cdot\sin(\mu_x).$$

The Jacobian is given by

$$J = \begin{bmatrix}\cos(\mu_x) & \sin(\mu_x)\\ -k_{2l}\cdot x\cdot\cos^2(\mu_x)-\sin(\mu_x) & -k_{2l}\cdot p_x\cdot\sin^2(\mu_x)+\cos(\mu_x)\end{bmatrix}.$$

Calculating the determinant of the Jacobian

$$\begin{aligned}\det(J) &= (\cos(\mu_x))\left(-k_{2l}\cdot p_x\cdot\sin^2(\mu_x)+\cos(\mu_x)\right)-(\sin(\mu_x))\left(-k_{2l}\cdot x\cdot\cos^2(\mu_x)-\sin(\mu_x)\right)\\ &= \cos^2(\mu_x)+k_{2l}\cdot p_x\cdot\sin^3(\mu_x)\cdot\cos(\mu_x)-k_{2l}\cdot x\cdot\sin(\mu_x)\cdot\cos^3(\mu_x)-\sin^2(\mu_x),\end{aligned}$$

which cannot be simplified to 1, indicating that the transformation is not be symplectic.

B.2 Exercice 2

Series truncation: the map of a quadrupole is given by

$$\mathcal{M}_Q = \begin{pmatrix}\cos(\sqrt{k}L) & \frac{1}{\sqrt{k}}\sin(\sqrt{k}L)\\ -\sqrt{k}\sin(\sqrt{k}L) & \cos(\sqrt{k}L)\end{pmatrix}, \tag{I.9.63}$$

which has a determinant of 1. From the Taylor expansion of the trigonometric functions

$$\cos(x) = 1-\frac{x^2}{2}+O(x^4), \tag{I.9.64}$$

$$\sin(x) = x-\frac{x^3}{6}+O(x^5). \tag{I.9.65}$$

Inserting the Taylor expansion of the trigonometric functions in the quadrupole map

$$\mathcal{M}_Q = \begin{pmatrix} 1 & L \\ -kL & 1 \end{pmatrix} + O(L^2). \tag{I.9.66}$$

Truncating terms higher than second order results in a determinant equal to $1 + kL^2$, which indicates a non-symplectic map. The map of the thin quadrupole is

$$M = \begin{pmatrix} 1 & 0 \\ -kL & 1 \end{pmatrix}, \tag{I.9.67}$$

which is symplectic.

References

[1] M. Tabor, *Chaos and integrability in nonlinear dynamics: An introduction* (Wiley, New York, NY, 1989).

[2] A. Lichtenberg, M. Lieberman, *Regular and chaotic dynamics* (Springer, New York, NY, 1992), doi:10.1007/978-1-4757-2184-3.

[3] E. Forest, *Beam dynamics: A new attitude and framework* (Harwood, Sidney, 1998).

[4] H. Wiedemann, *Particle accelerator physics*, 4th ed. (Springer, Cham, 2015), doi:10.1007/978-3-319-18317-6.

[5] A. Wolski, *Beam dynamics in high energy particle accelerators*, Imperial College Press, 2014, doi:10.1142/p899.

[6] A. Chao, Advanced topics in accelerator physics, pres. United States Particle Accelerator School (USPAS), 2000, SLAC-PUB-9574 (Revision 3 Jan. 2012), https://www.slac.stanford.edu/ achao/lecturenotes.html.

[7] A. Wolski, *Lectures on Non-linear dynamics in accelerators*, Cockroft Institute, 2015.

[8] R. Bartolini, *Lecture on Non-linear dynamics*, John Adams Institute, 2017.

[9] G. Guignard, The general theory of all sum and difference resonances in a three-dimensional magnetic field in a synchrotron, CERN 76-06 (CERN, Geneva, 1976), 10.5170/CERN-1976-006.

[10] G. Guignard, A general treatment of resonances in accelerators, CERN 78-11 (CERN, Geneva, 1978), doi:10.5170/CERN-1978-011.

[11] J. Bengtsson, Non-linear transverse dynamics for storage rings with applications to the low-energy antiproton ring (LEAR) at CERN, CERN-88-05 (CERN, Geneva, 1988), doi:10.5170/CERN-1988-005.

[12] H. Bartosik, Y. Papaphilippou, A. Wolski, A first taste of nonlinear beam dynamics, CERN Accelerator School: Introduction to Accelerator Physics, Chavannes de Bogis, 25 Sep.–8 Oct. 2021, doi:10.48550/arXiv.2201.01532.

[13] Y. Papaphilippou, Numerical analysis techniques for non-linear dynamics, in Proc. CERN Accelerator School: Course on Numerical Methods for Analysis, Design and Modelling of Particle Accelerators, Thessaloniki, Greece, 11–23 Nov. 2018, Edited by M. Filippova *et al.* (CERN, Geneva, 2020), pp. 209–235, doi:10.48550/arXiv.2012.10552.

[14] B. Chirikov, A universal instability of many-dimensional oscillator systems, *Phys. Rep.* **52** (1979) 263–379, 10.1016/0370-1573(79)90023-1.

[15] D. Robin *et al.*, Enhanced performance of the Advanced Light Source through periodicity restoration of the linear lattice, in Proc. 7th European Particle Accelerator Conference, Vienna, Austria, 26–30 Jun. 2000, pp. 136–140, JACoW.

[16] F. Asvesta *et al.*, Resonance compensation for high intensity and high brightness beams in the CERN PSB, in Proc. 64th ICFA Advanced Beam Dynamics Workshop on High Intensity and High Brightness Hadron Beams (HB 2021), Batavia, IL, United States, 4–9 Oct. 2021, pp. 40–45, doi:10.18429/JACoW-HB2021-MOP06.

[17] E. Maclean, Modelling and correction of the non-linear transverse dynamics of the LHC from beam-based measurements, Ph.D. thesis, Hertford College, Oxford, 2014, doi:10.17181/CERN-THESIS-2014-135.

[18] J. Laskar, The chaotic motion of the solar system: a numerical estimate of the size of the chaotic zones, *Icarus* **88** (1990) 266–291, doi:10.1016/0019-1035(90)90084-M.

[19] J. Laskar, Frequency map analysis of a Hamiltonian system, *AIP Conf. Proc.* **344** (1995) 130–159, doi:10.1063/1.48978.

[20] J. Laskar, Frequency map analysis and particle accelerators, in Proc. 2003 Particle Accelerator Conf. Portland, OR, USA, 12–16 May 2003, Edited by J. Chew, P. Lucas and S. Webbe (IEEE, Piscataway, NJ, 2003) vol. 1, pp. 378–382, doi:10.1109/PAC.2003.1288929.

[21] Y. Papaphilippou, Detecting chaos in particle accelerators through the frequency map analysis method, *Chaos* **24** (2014) 024412, doi:10.1063/1.4884495.

[22] J. Laskar, Introduction to frequency map analysis, *NATO ASI Series* **533** (1999) 134–150, doi:10.1007/978-94-011-4673-9_13.

[23] W. Herr and T. Pieloni, Beam-beam effects, in Proc. CERN Accelerator School: Advanced Accelerator Physics Course, Trondheim, Norway, 18–29 Aug. 2013, Edited by W. Herr, CERN-2014-009 (CERN, Geneva, 2014), pp. 431–459, doi:10.5170/CERN-2014-009.431.

[24] S. Kostoglou *et al.*, Tune modulation effects for colliding beams in the High Luminosity Large Hadron Collider, *Phys. Rev. Accel. Beams* **23** (2020) 121001, doi:10.1103/PhysRevAccelBeams.23.121001.

[25] S. Fartoukh *et al.*, Compensation of the long-range beam-beam interactions as a path towards new configurations for the high luminosity LHC, *Phys. Rev. ST Accel. Beams*, **18** (2015) 121001, doi:10.1103/PhysRevSTAB.18.121001.

[26] A. Huschauer *et al.*, Advancing the CERN proton synchrotron multiturn extraction towards the high-intensity proton beams frontier, *Phys. Rev. Accel. Beams*, **22** (2019) 104002, doi:10.1103/PhysRevAccelBeams.22.104002.

[27] R. Cappi, M. Giovannozzi, Novel method for multi-turn extraction: Trapping charged particles in islands of phase space, *Phys. Rev. Lett.* **88** (2002) 104801, doi:10.1103/PhysRevLett.88.104801.